Delft University of Technology

Optimization of adaptive metal foam arrangement in a heat storage tank

Guo, Junfei; Li, Ze; Wei, Pan; Li, Ling; Yang, Xiaohu; He, Ya Ling; Hooman, Kamel

Important note
To cite this publication, please use the final published version (if applicable).
Please check the document version above.

Optimization of adaptive metal foam arrangement in a heat storage tank

Junfei Guo[a], Ze Li[a], Pan Wei[a,b], Ling Li[a], Xiaohu Yang[a,c,*], Ya-Ling He[c], Kamel Hooman[d]

[a] *Institute of the Building Environment & Sustainability Technology, School of Human Settlements and Civil Engineering, Xi'an Jiaotong University, Xi'an 710049, China*

[b] *China Northwest Architecture Design and Research Institute, CO. Ltd, Xi'an 710077, Shaanxi Province, China*

[c] *Key Laboratory of Thermo-Fluid Science and Engineering of Ministry of Education, School of Energy and Power Engineering, Xi'an Jiaotong University, Xi'an, Shaanxi 710049, China*

[d] *Process & Energy Department of the 3mE Faculty, Delft University of Technology, Delft, the Netherlands*

ARTICLE INFO

ABSTRACT

The integration of phase change materials (PCMs) and metal foam has been widely concerned recently. To decrease non-uniformity of uniform metal foam-PCMs, adaptive metal foam arrangement strategy with increasing porosity from inside to outside has attracted widespread attention. This work conducted a symmetric simulation model of vertical thermal energy storage (TES) tube validated by experiments, for optimization of adaptive metal foam arrangement in basic design (0.94–0.94–0.94). It was followed by assessing the performance of gradient metal foam structures that included 27 cases with radial foam gradients of larger porosity on the outside and smaller porosity on the inside. Results demonstrated that a smaller difference between the inside and outside subregions resulted in better thermal performance when the same porosity of the intermediate subregion was used. More intense natural convection with stronger liquid paraffin vortex could be obtained by an adaptive arrangement. With the same average porosity, the faster phase change evolution, which was influenced by the maximum promotion of stronger natural convection, was achieved by using a larger intermediate porosity and a larger porosity difference between the inside and outside regions. The optimal strategy (0.87–0.94–0.97) could significantly shorten the melting duration as maximal as 17.15% compared with the original uniform (0.94–0.94–0.94), which contributed to efficient vertical metal foam TES systems, also as light and cost-effective as possible while also avoiding sacrificing thermal capacity.

© 2023 Elsevier Ltd. All rights reserved.

1. Introduction

Considering that thermal energy production and supply are inconsistent in intensity, time, and space, thermal energy storage (TES) system is widely used to provide a reliable thermal bank [1–3]. Thermal energy storage may be classified into three forms based on various principles: sensible [4,5], latent [6–8], and thermochemical [9,10]. Latent thermal energy storage (LTES) with the advantages of higher TES density has emerged as the most widely-used in different engineering fields [11–14]. Specifically, the outstanding performance of LTES was demonstrated by Ghoneim et al. [15] in 1989, and the phase change materials (PCMs) have the potential to accommodate 5 to 14 times more heat than traditional sensible thermal energy storage materials.

However, the heat transfer of PCMs is deteriorative due to their low thermal conductivity [16,17]. It is proposed to effectively deal with this problem through additive with high thermal conductivity, such as fins [18,19], metal foam [20,21], nanomaterials [22]. Among them, metal foam is an attractive way to optimize the heat transfer, forming the high-performance composite PCM, attributed to its larger specific surface area, finer thermal penetration ability and greater thermal conductivity [23,24]. The integration of PCMs and metal foam has attracted widespread attention these days, serving an essential role in solar thermal collector [25], industrial waste heat recovery [26], thermal management [22,27,28], by a considerable number of investigations. Wang et al. [29] experimentally analyzed the influence of metal foam on energy storage systems performance. It was revealed that the integration of metal foam could shorten the melting time and avoid thermal backlog in some regions with thermal poorness in others, which was beneficial for developing thermal energy storage for the exploitation of solar energy at medium temperatures. Prasanth et al. [30] conducted a modified heat storage tank with thermal volume of 300 KJ, filling

Nomenclature

Abbreviation

CFPCM	Copper foam phase change material
FVM	Finite volume method
HTF	Heat transfer fluid
HTT	Heat transfer tube
PCM	Phase change material
PPI	Pores per inch
TES	Thermal energy storage

Symbols

C_E	Inertial coefficient
C_s	Small computational constant
c_p	Specific heat ($J \cdot kg^{-1} \cdot K^{-1}$)
d	The average ligament diameter of open-cell foam (m)
ER	Enhancement ratio
e	Thickness ratio of node to solid ligament
f	Friction factor
f_m	Melting fraction
G	Shape function for metallic ligaments
g	Acceleration of gravity ($m \cdot s^{-2}$)
h_{sf}	Interstitial heat transfer coefficient ($W \cdot m^{-2} \cdot K^{-1}$)
K	Permeability
k	Thermal conductivity ($W \cdot m^{-1} \cdot K^{-1}$)
k_{td}	Thermal dispersion coefficient ($m^2 \cdot s^{-1}$)
L	Latent heat ($kJ \cdot kg^{-1}$)
p	Pressure (Pa)
q	Heat flux ($W \cdot m^{-2}$)
$\overline{q}$	Average heat flux ($W \cdot m^{-2}$)
$\overline{RR}$	Integral average temperature response rate ($°C \cdot s^{-1}$)
T	Temperature ($°C$)
t	Time (s)
U	Velocity ($m \cdot s^{-1}$)
u	Superficial velocity at x direction ($m \cdot s^{-1}$)
v	Superficial velocity at y direction ($m \cdot s^{-1}$); Average velocity ($m \cdot s^{-1}$)
w	Superficial velocity at y direction ($m \cdot s^{-1}$)
v_{fm}	Variation rate of liquid fraction

Greek symbols

β	Thermal expansion coefficient (K^{-1})
ε	Porosity
α_{sf}	Specific area (m^{-1})
μ	Dynamic viscosity ($kg \cdot m^{-1} \cdot s^{-1}$)
ρ	Density ($kg \cdot m^{-3}$)
σ	Liquid fraction liquid in the porous medium
σ_{fm}	Melting evenness index
χ	Flow tortuosity
Ω	Vorticity (s^{-1})

Subscript

ave	Average
in	Inside subregion near the heat transfer tube
m	Melted PCM; Intermediate subregion; Melting time
out	Outside subregion far from the heat transfer tube
s	PCM in solid phase; Subregions

with composite PCMs consisting industrial paraffin and metal foam. Experimental results showed that the thermal efficiency of the metal foam-PCM heat tank ranged from 60 % to 85 % under different common heat transfer fluids. Ali et al. [31] proposed a integrative heat sink as thermal management device adopting the copper foam, phase change material and heat pipe. It was exper-

imentally concluded that the hybrid cooling could led to a more effective thermal dissipation in comparison to other traditional approaches under 2 and 3 kW/m² for the same operating duration. Veismoradi et al. [32] used the integration of copper foam and PCMs for the cooling of Li-ion battery packs. It was demonstrated that the greater thermal load due to higher electrical power was corresponded to the higher efficiency. The improvement of seven times could be realized, which was attributed to the metal foam.

The metal foam-PCM with uniform arrangement melting process evolves in a non-uniform manner due to the heat transfer process impacted by temperature distribution and the development of natural convection limited by the porous structure [33]. As a result, several studies propose gradient metal foam designs with variable porosity and pore density (PPI) [34–36]. Mahdi et al. [37] invoked a multiple-segment metal foam arrangement alongside the orientation of heat flow in the horizontal shell-and-tube TES tube. Their numerical outcomes reported that the charging and discharging rates could be significantly accelerated by metal foam with varying porosity. Ghahremannezhad et al. [38] employed the Darcy-Brinkman-Forchheimer model to simulate the influence of variable metallic foam on the phase change process. Results show that the gradient porous could promote melting rate and uniformity of temperature distribution. Meanwhile, the optimization could be observed under various heating supplies and at the whole charging stages. Marri et al. [39] experimentally and numerically examined melting performance of shell-and-tube heat sink immersed with gradient metallic foam during the cycles of energy storage and release. It was indicated that when with constant porosity, the sink with the non-uniform PPI density, that is higher at top than bottom, outperformed the uniform foam configurations in melting rate as much as 45 %. Zhuang et al. [40] conducted a three-dimensional numerical model, that is validated by PIV experimental images, to explore the influence of linear metallic foam on thermal energy storage performance. It was noted that phase change heat transfer was comprehensively affected by thermal conduction and natural convection caused by the non-uniform metal foam. Ahmadi et al. [41] employed a 2D model to predict the performance of the metal foam-PCM thermal energy storage units for concentrated solar power plants. It was verified that the total entropy generation was enhanced by 7.96 % in optimized configuration compared with the original structure.

It should be noted that most of the above studies just simply showed the superiority of gradient metal foam-PCM. Optimized gradient direction has received a lot of attention, but there still is a lack of more clear studies on the influence of non-uniform morphologies (that is porosity gradient difference) of metallic foam on the thermal behaviors of vertical shell-and-tube TES units. The coordination between the layout of metal foam and heat transfer process deserves more attention. This work studied an adaptive metal foam layout to achieve a better comprehensive performance of LTES unit, and analyzed the effect of porosity variation differences on strengthening.

2. Physical model and mathematical modeling

2.1. Physical model

Fig. 1(a) depicted a schematics of vertical shell-and-tube TES tank with an inner diameter of 22 mm, an outside diameter of 90 mm and height of 270 mm, embedding with an adaptive metal foam arrangement. A composite PCM made up of copper foam with a fixed PPI of 15 and paraffin wax with the melting temperature range of 53–54 °C, named as copper foam phase change material (CFPCM). Hot water of 70 °C and 0.05 m·s⁻¹ flowing through heat transfer tube (HTT) represented heat transfer fluid
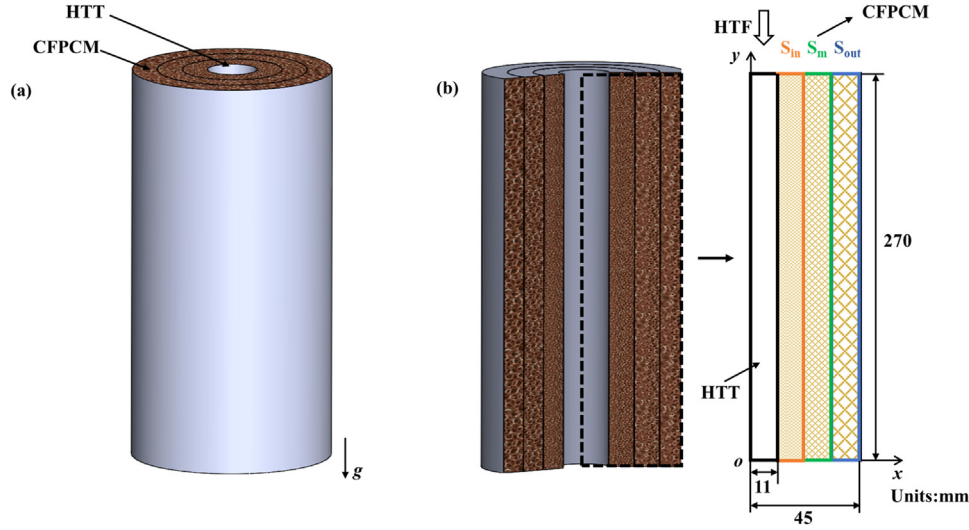
Fig. 1. (a) Schematics of adaptive metal foam arrangement in vertical thermal energy storage tube and (b) computer domains

Table 1
Physical parameters of paraffin and copper [42].

	P kg·m^{-3}	c_p J·kg^{-1}·K^{-1}	k W·m^{-1}·K^{-1}	β K^{-1}	μ kg·m^{-1}·s^{-1}	L kJ·kg^{-1}	T_m °C
Paraffin	850(solid)/ 800(liquid)	2000	0.2(solid)/ 0.1(liquid)	7.5×10^{-4}	2.51×10^{-3}	200	53–54
Copper	8920	380	401				

(HTF). Table 1 listed the thermophysical properties of the materials.

Directed by the adaptive metal foam strategy, the metal foam with a radial obliquity of larger porosity on the outside and smaller porosity on the inside was used to solve the melting characteristic of poor heat transfer on the outside than inside. Total PCM area was divided into three subregions with the same area as S_{in}, S_m and S_{out}, filling with metal foam with the porosity of ε_{in}, ε_m and ε_{out}. Considering the axisymmetric characteristics of shell-and-tube and time cost of simulation, the computer domain was simplified as two-dimensional model consisting of CFPCM and HTT, as shown in Fig. 1(b).

2.2. Governing equations

To develop the mathematical model, some essential assumptions were stated as follows. The Boussinesq approximation was used to determine the density change, with considering the liquid paraffin as an incompressible Newtonian fluid. Metal foam and paraffin were thought of as continuous media. It was ignored to account for heat resistance between several copper foam layers. Paraffin's change in heat capacity while melting was disregarded.

The following were the governing equations that can be applied to calculate phase change heat transfer of CFPCM. Based on the hypothesis mentioned earlier above.

Continuity equation:

$$\frac{\partial \rho_f}{\partial t} + \nabla \cdot \left(\rho_f \left\langle \vec{U} \right\rangle \right) = 0 \tag{1}$$

Momentum equations:

$$\frac{\rho_f}{\sigma} \frac{\partial \langle u \rangle}{\partial t} + \frac{\rho_f}{\sigma^2} \left(\langle \vec{U} \rangle \cdot \nabla \right) \langle u \rangle$$
$$= -\frac{\partial \langle p \rangle}{\partial x} + \frac{\mu_f}{\sigma} \nabla^2 \langle u \rangle - \left(\frac{\mu_f}{K} + \frac{\rho_f C_E}{\sqrt{K}} \left| \langle \vec{U} \rangle \right| \right) \langle u \rangle - \frac{(1 - f_m)^2}{f_m{}^3 + \delta} A_m \langle u \rangle \tag{2}$$

$$\frac{\rho_f}{\sigma} \frac{\partial \langle v \rangle}{\partial t} + \frac{\rho_f}{\sigma^2} \left(\langle \vec{U} \rangle \cdot \nabla \right) \langle v \rangle = -\frac{\partial \langle p \rangle}{\partial y} + \frac{\mu_f}{\sigma} \nabla^2 \langle v \rangle - \left(\frac{\mu_f}{K} + \frac{\rho_f C_E}{\sqrt{K}} \left| \langle \vec{U} \rangle \right| \right) \langle v \rangle$$
$$- \frac{(1 - f_m)^2}{f_m{}^3 + \delta} A_m \langle v \rangle + \rho_f g \beta \left(\langle T_f \rangle - T_{m1} \right) \tag{3}$$

$$\frac{\rho_f}{\sigma} \frac{\partial \langle w \rangle}{\partial t} + \frac{\rho_f}{\sigma^2} \left(\langle \vec{U} \rangle \cdot \nabla \right) \langle w \rangle$$
$$= -\frac{\partial \langle p \rangle}{\partial x} + \frac{\mu_f}{\sigma} \nabla^2 \langle w \rangle - \left(\frac{\mu_f}{K} + \frac{\rho_f C_E}{\sqrt{K}} \left| \langle \vec{U} \rangle \right| \right) \langle w \rangle - \frac{(1 - f_m)^2}{f_m{}^3 + \delta} A_m \langle w \rangle \tag{4}$$

In Eq. (2), (3) and (4), the $\left(\frac{\mu_f}{K} + \frac{\rho_f C_E}{\sqrt{K}} \left| \langle \vec{U} \rangle \right| \right) \langle u \rangle$, $\left(\frac{\mu_f}{K} + \frac{\rho_f C_E}{\sqrt{K}} \left| \langle \vec{U} \rangle \right| \right) \langle v \rangle$ and $\left(\frac{\mu_f}{K} + \frac{\rho_f C_E}{\sqrt{K}} \left| \langle \vec{U} \rangle \right| \right) \langle w \rangle$ represented the influence by porous structure, which was the expression of the Forchheimer extended Darcy model. K and C_E were given as follows:

$$K = \frac{\varepsilon \left[1 - (1 - \varepsilon)^{1/3} \right]}{108 \left[(1 - \varepsilon)^{1/3} - (1 - \varepsilon) \right]} d_p{}^2 \tag{5}$$

$$C_E = 0.095 \frac{c_d}{12} \sqrt{\frac{\varepsilon}{3(\chi - 1)}} \left(1.18 \sqrt{\frac{1 - \varepsilon}{3\pi}} \frac{1}{G} \right)^{-1} \tag{6}$$

$$\chi = \frac{\varepsilon}{1 - (1 - \varepsilon)^{1/3}} \tag{7}$$

$$G = 1 - e^{-(1 - \varepsilon)/0.04} \tag{8}$$

And the $\frac{(1 - f_m)^2}{f_m{}^3 + \delta} A_m \langle u \rangle$ was employed to describe the influence of phase change evolution on the momentum. The liquid fraction
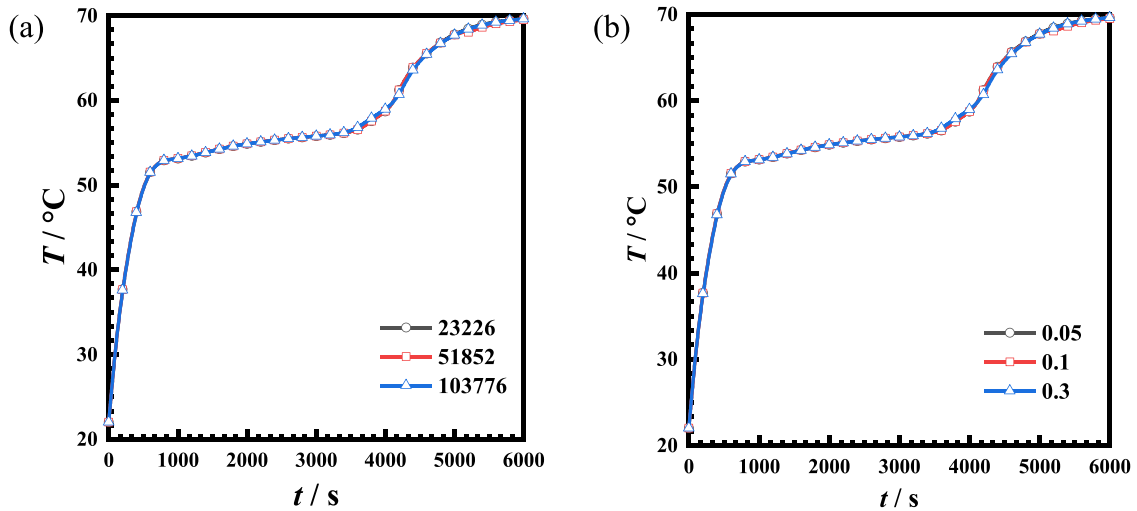
Fig. 2. The average temperature in total PCM region (T / °C) under (a) different grid numbers and (b) different time steps

f_m and the parameter for velocity damping A_m was calculated by:

$$f_m = \begin{cases} 0 & T_f < T_{m1} \\ \dfrac{T_f - T_{m1}}{T_{m2} - T_{m1}} & T_{m1} < T_f < T_{m2} \\ 1 & T_{m2} < T_f \end{cases} \tag{9}$$

$$A_m = \frac{C(1 - f_l)^2}{C_s + f_l^3} \tag{10}$$

where C was the mushy zone constant set to 10^5 [43], and C_s was a small computational constant as 10^{-3}.

Energy equation:

PCM:

$$\varepsilon \rho_f \left(c_{pf} + L \frac{df_l}{dt} \right) \frac{\partial \langle T_f \rangle}{\partial t} + \rho_f c_{pf} \langle \vec{U} \rangle \cdot \nabla \langle T_f \rangle$$
$$= \nabla \cdot \left(\left(k_{fe} + k_{td} \right) \nabla \langle T_f \rangle \right) - h_{sf} a_{sf} \left(\langle T_f \rangle - \langle T_s \rangle \right) \tag{11}$$
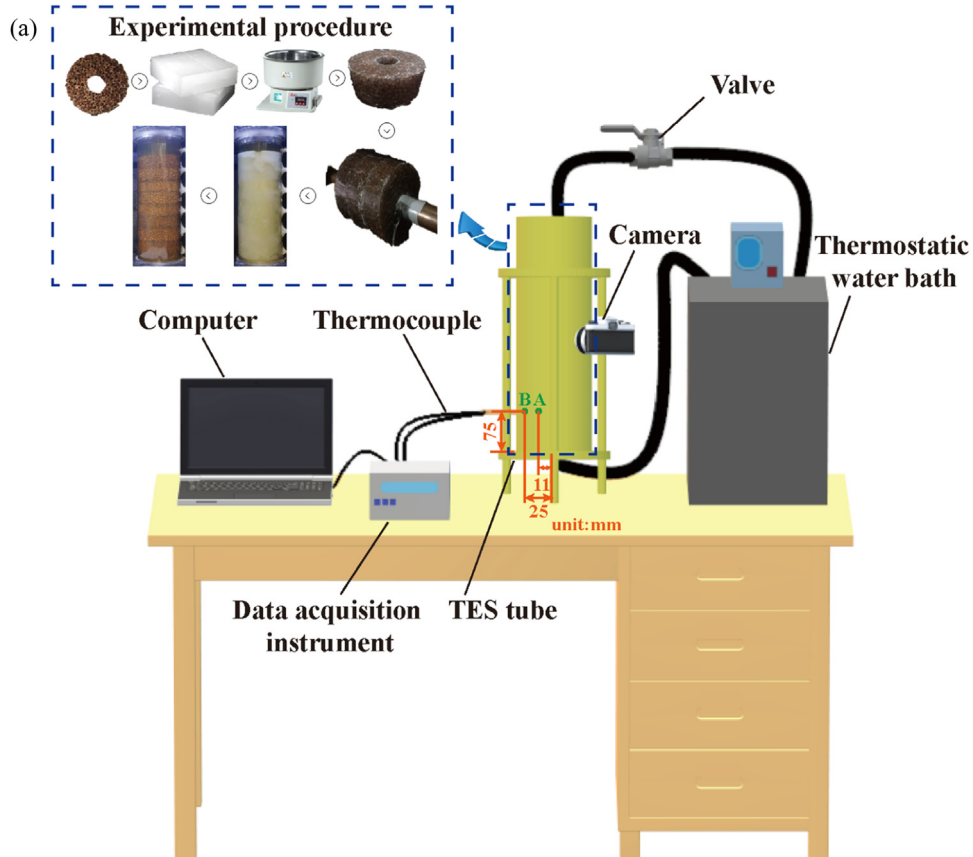

Fig. 3. (a) Experimental system, and comparison of (b) transient phase interface morphology and (c) transient-temperature (T / °C) at Point A and Point B between experiment and simulation
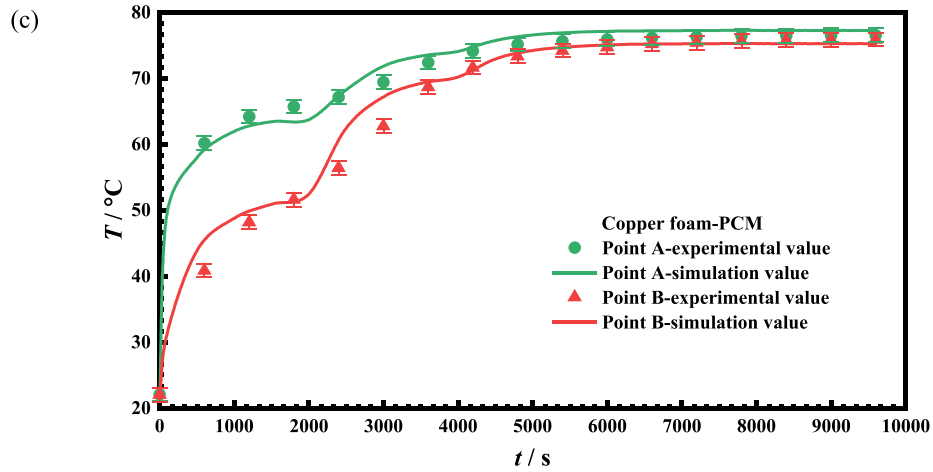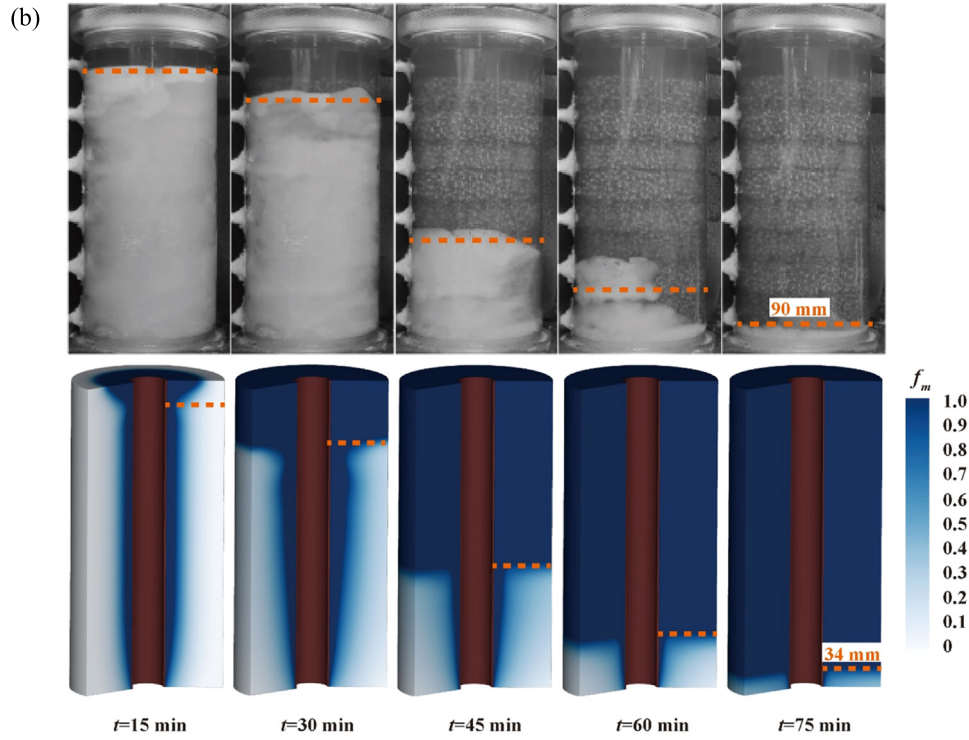
Fig. 3. Continued

The $\varepsilon\rho_f(c_{pf} + L\frac{df_l}{dt})$ represented the comprehensive heat transfer influences including sensible and latent heat of PCM, based on the enthalpy porosity mode.

Metal foam:

$$(1-\varepsilon)\rho_s c_{ps}\frac{\partial\langle T_s\rangle}{\partial t} = \nabla\cdot\left(k_{se}\nabla\langle T_f\rangle\right) - h_{sf}a_{sf}\left(\langle T_s\rangle - \langle T_f\rangle\right) \quad (12)$$

$$a_{sf} = \frac{1.18\omega}{0.0224}\sqrt{3\pi(1-\varepsilon)} \quad (13)$$

$$h_{sf} = \begin{cases} (0.35 + 0.5\text{Re}^{0.5})k_f/d_f, & 0 \leq \text{Re} \leq 1 \\ 0.76\text{Re}^{0.4}\text{Pr}^{0.37}k_f/d_f, & 1 < \text{Re} \leq 40 \\ 0.52\text{Re}^{0.5}\text{Pr}^{0.37}k_f/d_f, & 40 < \text{Re} \leq 1000 \\ 0.26\text{Re}^{0.6}\text{Pr}^{0.37}k_f/d_f, & 1000 < \text{Re} \leq 20000 \end{cases} \quad (14)$$

$$\sigma = \varepsilon f_l \quad (15)$$

The symbol $\langle\rangle$ in above equations denoted the volume average operation; h_{sf} and a_{sf} were calculated by [44,45].

2.3. Numerical procedure

The simulation calculations were carried out using ANSYS Fluent 19R3 software. The finite volume method (FVM) was used to accurately predict the phase change in porous structure. The enthalpy porosity technique was employed for the heat transfer of solid and liquid paraffin. The PRESTO! scheme was activated for the pressure correction and the SIMPLE algorithm was selected to solve the pressure-velocity coupling. The convergence criterion for the energy conservation equation, continuity equation, and momentum equation were remained smaller than 10^{-6}. The left boundary of the heat transfer tube (HTT) computation domain was set as the symmetry axis. The junction of HTT and CFPCM was coupled. The boundary of HTF inflow and outflow were considered as the inlet and outlet respectively. And the rest of the boundary

was set as adiabatic, ignoring the thermal disturbance of the surrounding environment. The primitive temperature of the vertical TES tube was 22 °C.

To assure a grid-independent solution, three available structured grids (23,226, 51,852, and 103,756 cells) were investigated. It was shown in Fig. 2(a) that the grids project of 51,852 cells was chosen, because it exhibited the maximum of a 1.04 % difference value compared with more grids and made lower the computer cost. Furthermore, three different time steps (0.05 s, 0.1 s, and 0.3 s) were also tested to ensure the accuracy of the results. As Fig. 2(b), the 0.1 s time step was found to be enough to adequate for the simulation, independent and stable over the phase change process.

3. Model validation

3.1. Experimental device

To verify simulation reliability of describing metal foam-PCMs melting action, a simple experimental test system was set up as Fig. 3(a), consisting of a thermostatic water bath (German, JULABO, CORIO CD-1001F) as heat source, a vertical shell-and-tube phase change thermal storage tube filled with paraffin (T_m = 53∼54 °C)(produced by Hualing company in Shanghai, China) and infused with metal foam (0.97 porosity and 10 PPI pore density, produced by Hefei Institutes of Physical Science, Chinese Academy of Sciences) placed by support frame, and corresponding equipment for thermocouple temperature measurement including computer (American, Dell), thermocouple (American, Omega, TT-K-30) and data acquisition instrument (China, KEYSIGHT, model 34,970 A), and necessary pipes and valves. Specifically, the test TES tube, which stood 300 mm tall, was constructed from a transparent plastic cylinder (an inner diameter of 85 mm and an outer diameter of 95 mm), coupled with a copper tube (an inner diameter of 20 mm and a wall thickness of 1 mm).

3.2. Experimental procedure

First, the non-standard copper foam block was created by wire cutting, as seen in Fig. 3(a). After that, put the paraffin and copper foam in the vacuum tank. The gage pressure is lowered to 0.01 MPa by a vacuum pump as the vacuum tank is placed in the water bath and maintained at 100 °C for two hours. After these operations, the PCM is fully melted. To guarantee that the PCM has fully frozen, the vacuum tank is then removed and allowed to cool to ambient temperature. Finally, remove the excess paraffin. The composite phase change material and copper pipe were assembled, and the copper pipe surface was coated with thermal conductive glue to reduce the contact thermal resistance of the composite phase change material and copper pipe. Considering the influence of heating power, pump work and room temperature of the experimental system, the oft-repeated tests were carried out with the conditions as hot water of 80 °C at 0.3 m/s by setting thermostatic water bath and adjusting the valve, and the initial temperature of 21 °C.

The transient phase interface morphology was captured, and compared with the numerical phase change evolution, as shown in Fig. 3(b). The consistent melting interface height qualitatively verified the reliability of the numerical model. The transient data of the two temperature measurement points at A and B (as shown in Fig. 3(a)) were extracted and adopted to compare with the corresponding numerical simulation results. The comparison in Fig. 3(c) revealed that the simulated temperature curve agreed well with the experimental tested results with less than 5 % miss-distance, which indicated that the numerical methods has reliably been calculated.

4. Results and discussion

To study the impact of adaptive metal foam arrangement on the thermal performance in vertical thermal energy storage tube, the porosity of metal foam was changed from inside to outside along radial orientation. The uniform CFPCM tube with the porosity of 0.94 was regarded as benchmark case. Then a series of cases with adaptive metal foam acceptably ranging between the porosity of 0.86 and 0.99 with a constant pore density of 15PPI were conducted by first determining the porosity of the intermediate region, followed by the properties of the inner and outer regions. According to adaptive metal foam arrangement, the outer region had the largest porosity, followed by the intermediate and the in-
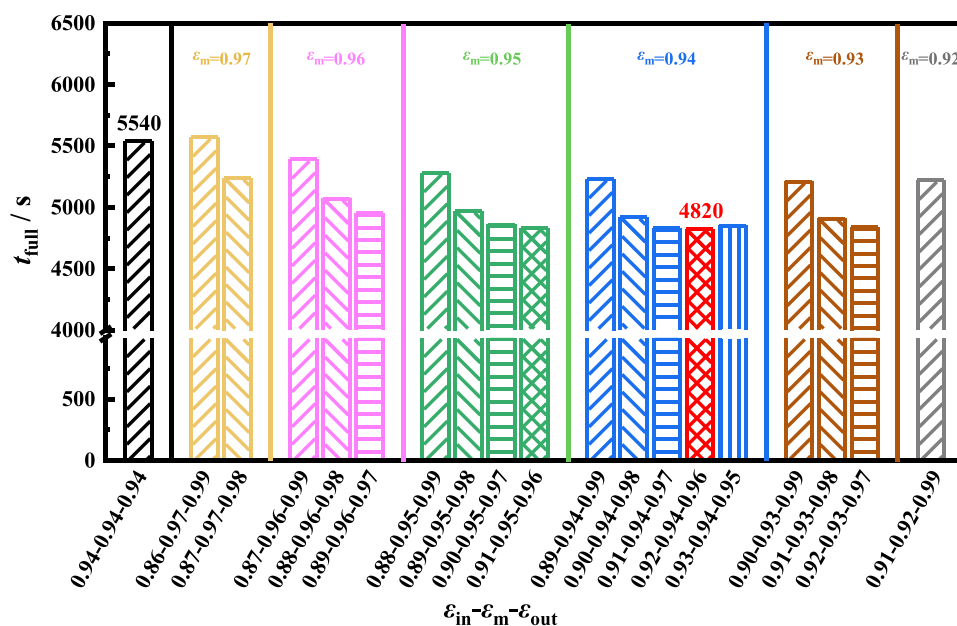

Fig. 4. Melting time (t_{full} / s) of vertical TES tube with uniform and adaptive non-uniform metal foam arrangement

Table 2
The metal foam porosity morphologies of adaptive metal foam arrangement.

	ε_{in}	ε_{m}	ε_{out}
case1	0.86	0.97	0.99
case2	0.87	0.97	0.98
case3	0.87	0.96	0.99
case4	0.88	0.96	0.98
case5	0.89	0.96	0.97
case6	0.88	0.95	0.99
case7	0.89	0.95	0.98
case8	0.90	0.95	0.97
case9	0.91	0.95	0.96
case10	0.89	0.94	0.99
case11	0.90	0.94	0.98
case12	0.91	0.94	0.97
case13	0.92	0.94	0.96
case14	0.93	0.94	0.95
case15	0.90	0.93	0.99
case16	0.91	0.93	0.98
case17	0.92	0.93	0.97
case18	0.91	0.92	0.99

ner region had the smallest. Table 2 enumerated the graded metal foam porosity morphologies.

Fig. 4 showed melting time of vertical TES tube with uniform and adaptive non-uniform metal foam arrangement. Limited by the acceptable range of metal foams used in each region, the porosity of the intermediate subregion varied from 0.92 to 0.97. According to the intermediate porosity the non-uniform metal foams could be divided into six groups. It was observed visually that compared with the original 0.94–0.94–0.94 structure, the gradually increasing porosity from the inside to the outside could effectively solve the problem of poor heat transfer of the TES tube, which indicated the advantages of adaptive metal foam strategy. The optimal metal foam layout for achieving the maximum melting rate, with the inside porosity of 0.92, the intermediate porosity of 0.94 and the outside porosity being 0.96, which reduced the melting duration by 13.00 % with 4820 s compared with 5540 s of the traditional uniform structure [46]. It could also be found that in the graded structure of each group based on the porosity of the intermediate region, there was a gradual trend in melting time, so that a minimum value with a proper difference within the group could be found. To further analyze the influence of porosity morphology in adaptive arrangement on melting development, temperature distribution and uniformity of thermal characteristics of vertical TES tube, uniform structure with 0.94–0.94–0.94 (case 1) and non-uniform designs with 0.89–0.94–0.99 (case 10) and 0.92–0.94–0.96 (case 13) from the ε_{m}=0.94 group, were selected to subsequent discussion, named as case A, case B and case C, respectively.
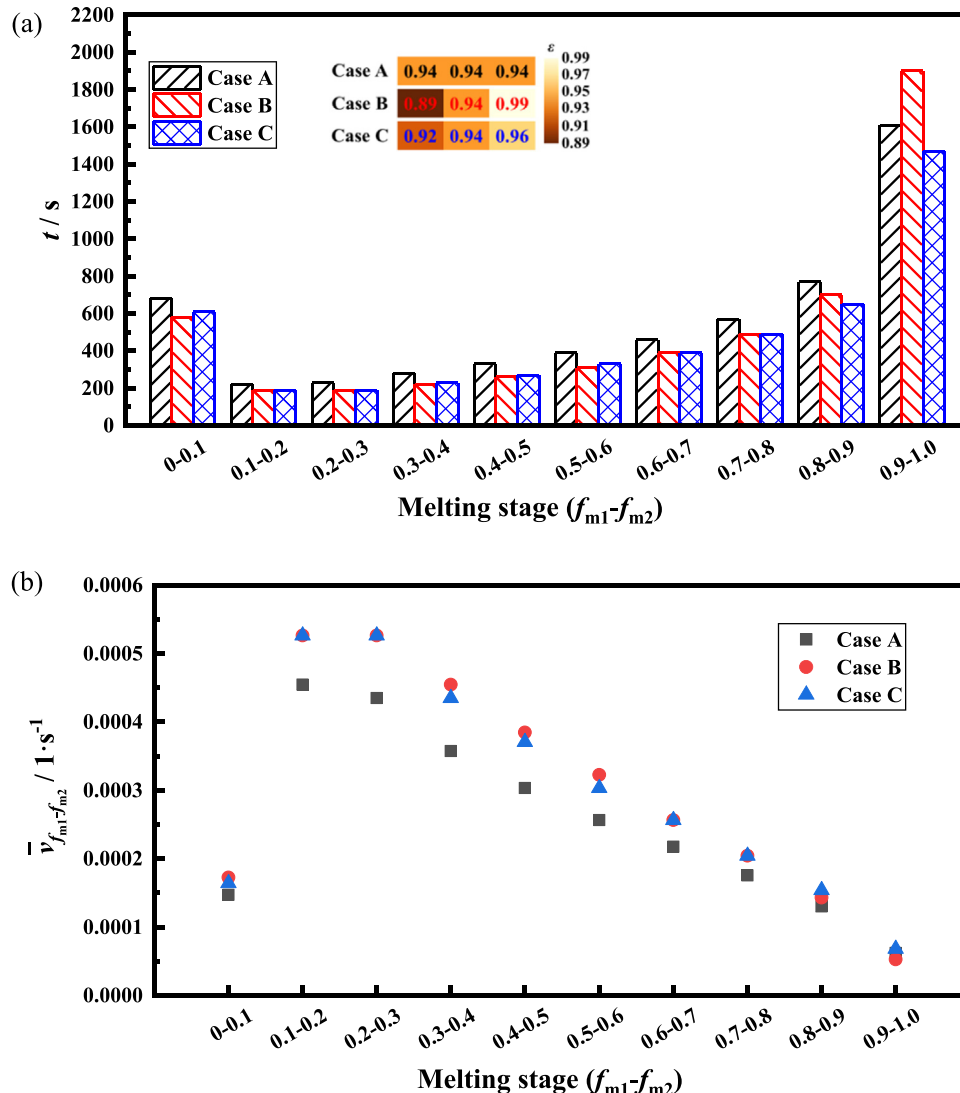

Fig. 5. (a) Melting time (t_{full} / s) and (b) liquid fraction variation rate ($\overline{v}_{f_{m1}-f_{m2}}$ / 1·s^{-1}) of different melting stages in vertical TES tube with uniform (case A) and adaptive non-uniform metal foam arrangement (case B and C)
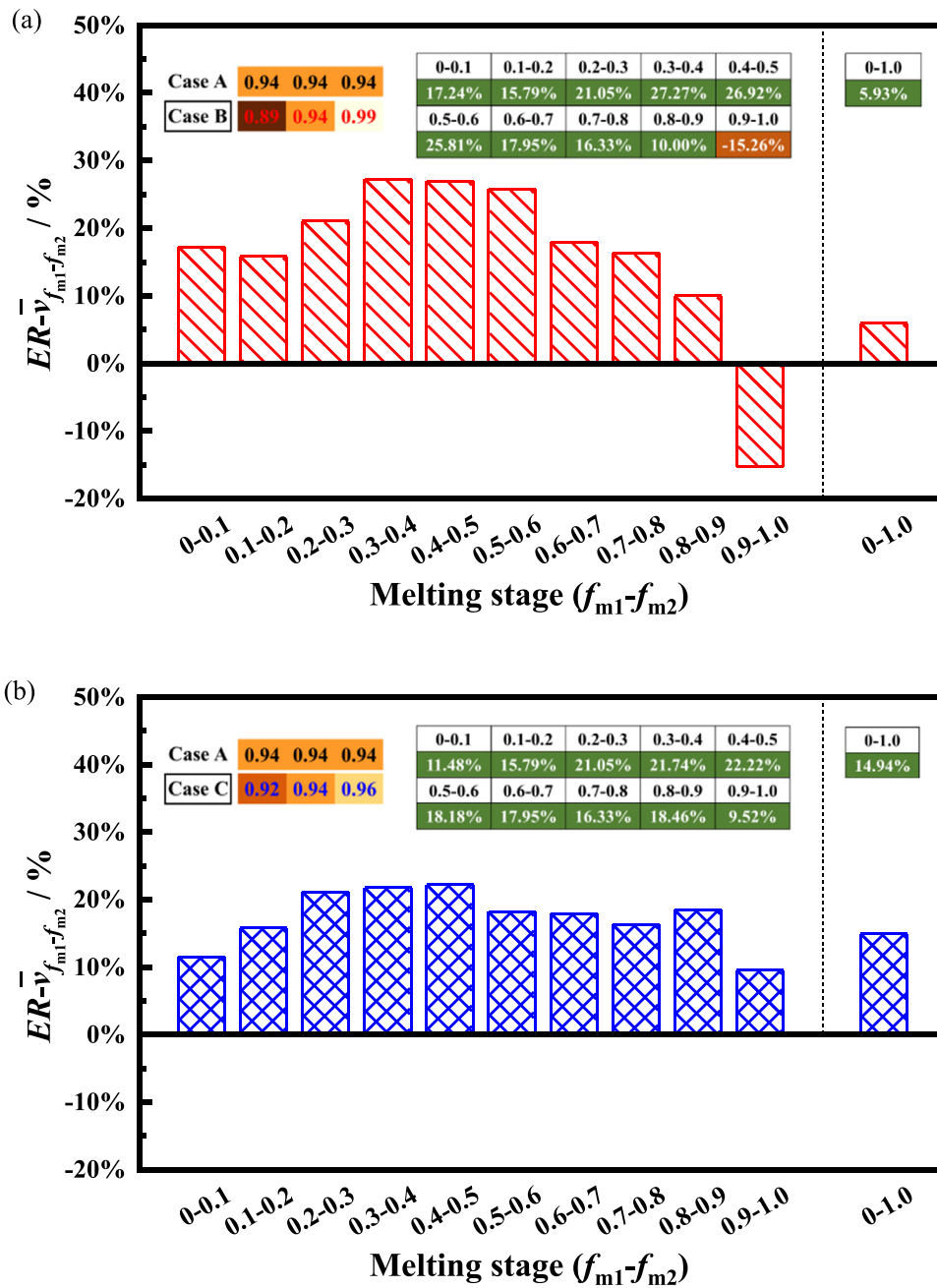
Fig. 6. Liquid fraction variation rate enhancement ratio ($ER - \overline{v}_{f_{m1}-f_{m2}}$ / %) (compared with uniform case A) in vertical TES tube with adaptive non-uniform metal foam arrangement ((a) case B and (b) case C)

4.1. Melting performance

Fig. 5(a) depicted the melting time for increasing the melting rate with each 0.1 increase during the whole phase change material, in vertical TES tube with uniform (case A) and adaptive non-uniform metal foam arrangements (case B and C). It was reported in case A that melting behavior took the longest in stages 0–0.1 (i.e., the initial melting phase) and 0.9–1.0 (i.e., the final melting phase), which were caused by weak heat conduction in the initial stage and low natural convection intensity in the final stage, respectively. Heat conduction and natural convection were effectively enhanced by adaptive non-uniform metal foam arrangement in case B and case C, illustrated by the less melting time. It was also pointed out from Fig. 5(b) that liquid fraction variation rate of different melting stages showed a trend of initially increasing

and then decreasing, resulting in the most difficult part of promoting melting as the late stage of melting (0.9–1.0). It's worth noting that the optimal adaptive non-uniform arrangement with the proper metal foam morphology (case C) outperformed primary adaptive design (case B) and uniform (case A).

To quantitatively illustrate the necessity of optimization of adaptive metal foam arrangement in vertical thermal energy storage tube, liquid fraction variation rate enhancement ratio, compared with uniform design case A, of vertical TES tube with adaptive non-uniform metal foam arrangement in case B and case C was shown as Fig. 6. The left part of the dotted line was the strengthening effect of the melting fraction in different stages for each 0.1 increment, and the right part of the dotted line was the whole melting process. It was demonstrated that liquid fraction variation rate during the whole melting process (0–1.0) was both

enhanced, compared with the traditional uniform structure [46], by adaptive non-uniform metal foam arrangement, as much as 5.93% in case B and 14.94 % in case C. It was found that optimized configurations case C exhibited promoted melting rate during the whole melting evolution with noticeable enhancement. As for case B, it unfortunately reduced the melting rate by 15.26 % in the melting stage (0.9–1.0), although it has a good promotion effect in other stages. It was revealed that non-uniform foam arrangement was differently influenced the melting performance in different melting stages.

Fig. 7(a) depicts the melting fraction and variation rate of liquid fraction in total PCM of case A, case B and case C. It was noted that case B and case C outperformed case A during the whole melting process with significant higher liquid fraction and shorting time. From the beginning of melting to the first half stage of the melting process of about 2300 s, the adaptive metal foam arrangement showed faster melting development, which was due to the emergence of more and more liquid phase PCM influenced by high thermal conductivity metal foam, and subsequently the development of natural convection became more and more intense. Case C achieved a comprehensive optimization of two main heat transfer methods, thanks to the non-uniform metal foam morphol-

ogy characteristics that were more suitable for the non-uniform thermal characteristics of the vertical TES tube. In the subsequent charging, due to the combined strengthening effect of heat conduction and natural convection presented in case B and case C, a higher melting fraction was obtained before 2300s, which provided a good foundation for the outside melting.

Fig. 7(b), (c) and (d) showed the melting fraction and variation rate of liquid fraction in S_{in}, S_m, and S_{out} subregions, separately. As shown in Fig. 7(b), because the inner region was the closest to the heat source, its melting performance was always faster than the other regions. Therefore, the advantage of case B and case C was not concentrated in the inner side. Nevertheless, the acceleration of melting was still ahead of case A with single structure metal foam throughout the melting process in this region.

As shown in Fig. 7(c), for the intermediate subregions, even though the same porosity 0.94 metal foam was arranged in three arrangements, the gradient metal foam showed significant advantages compared to the original structure. To be specific, case B with 0.89–0.94–0.99 surpassed the initial structure due to higher initial melting rate influenced by the more efficient heat conduction by smaller inside porosity in inside subregion. Case C with 0.92–0.94–0.96 exceeded the initial structure was
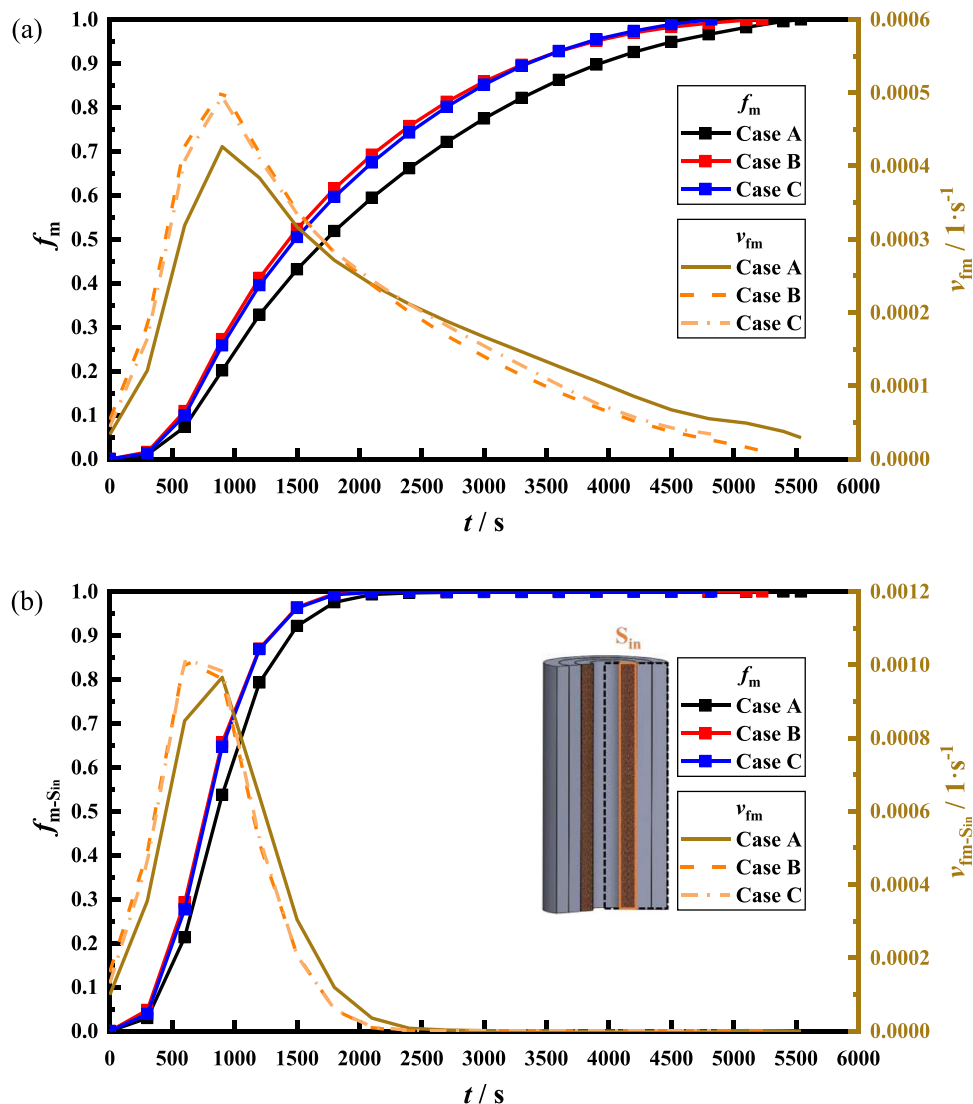

Fig. 7. Melting fraction f_m and variation rate of liquid fraction (v_{f_m}/ $1 \cdot s^{-1}$) in (a) total PCM region, (b) S_{in}, (c) S_m and (d) S_{out} of vertical TES tube with uniform (case A) and adaptive non-uniform metal foam arrangement (case B and case C)
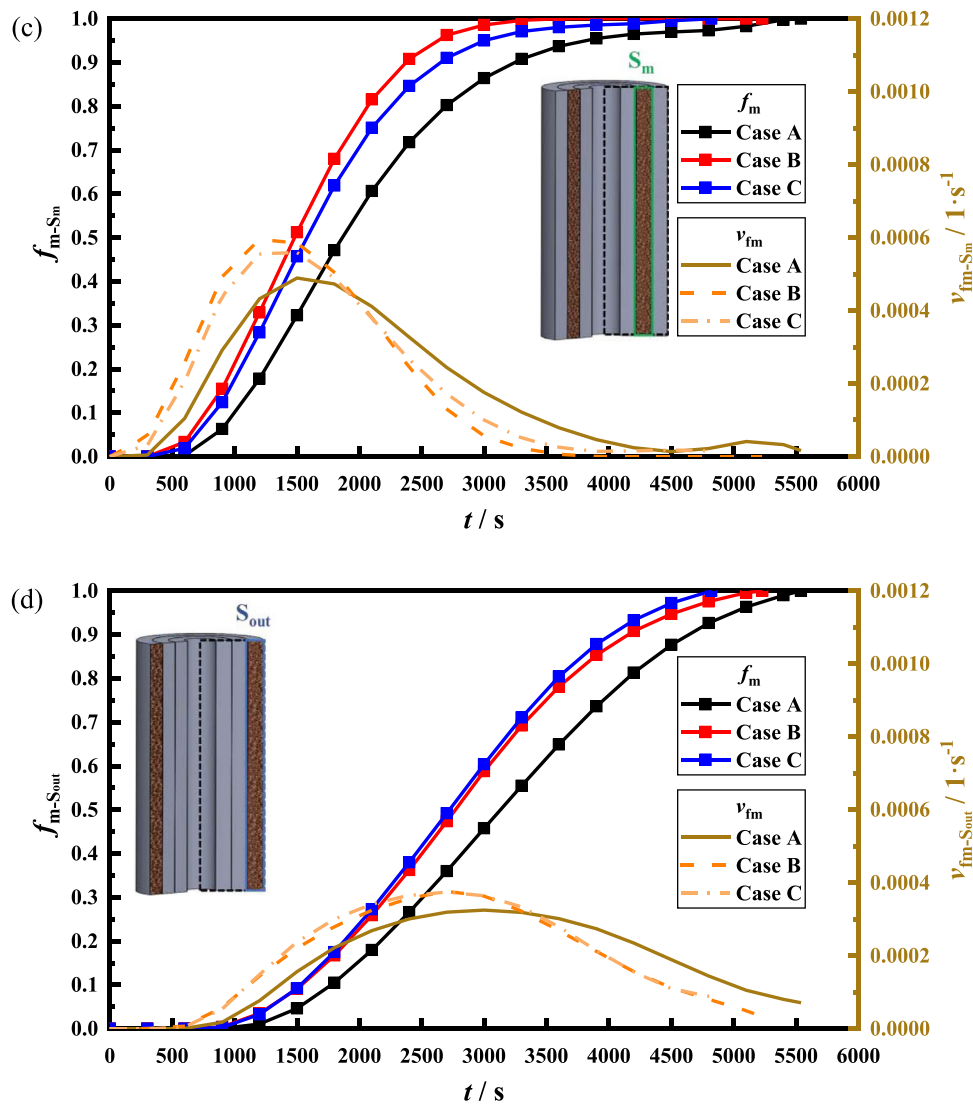
Fig. 7. Continued

attributed to intensification of the later stages of the melting process with stronger natural convection of whole PCM by larger outside porosity. When it comes to the melting enhancement in outside region, it has received considerable critical attention due to the farer thermal distance from heat source and thermal resistance. The melting development in the outer region depended on the appearance of large amounts of liquid phase in other regions, leading the intensification of natural convection as the main target. Considering the metal foam with high thermal conductivity due to its metallic framework and restriction of flow due to its porous structure, metal foam with higher porosity was applied for acceleration of nature convection development in outside subregion. It was stated in Fig. 7(d) that case C exhibited the fastest charging rate in outside ahead of case A and case B.

Fig. 8 depicted phase change behavior of vertical TES tube with uniform (case A) and adaptive non-uniform metal foam arrangement (case B and C) at $t = 1000$ s, 2000 s, 3000 s and 4000 s. At $t = 1000$s, the solid paraffin in the inside subregion adjacent to the HTT wall started to melt first and had a tilted phase interface due to the natural convection effect. The melting front developed almost along the radial direction from the HTT wall to the TES tube wall, which was the most important reason for the adaptive metal foam arrangement. The solid-liquid interface forward of

case B and case C was more able to reach the region farther away from the heat source compared to case A. With the development of melting, a large amount of melted paraffin had already appeared in the inner and middle regions, as the images of $t = 2000$ s. When $t = 3000$ s, the outer region started to melt. Case C obviously had a more rapid melting process compared to case B and case A. At $t = 4000$ s, the end of the melting process, only a small part of the un-melted paraffin in case C was left at the outermost corner, while the area of the un-melted region in case A was about three times that of case C.

The melting uniformity index is applied to further quantitatively illustrate melting performance of different gradient copper foam tubes, which is defined as follows:

$$\sigma_{f_m}(t) = \sqrt{\frac{1}{n} \sum_{i=1}^{n} \left[f_{m,S_i}(S_i, t) - f_{m,average}(t) \right]^2} \tag{16}$$

where $f_{m,Si}$ and $f_{m,average}$ are the melting rate at different subregion and the average melting rate of the heat storage unit. Fig. 9 showed transient melting evenness index of vertical TES tube with uniform (case A) and adaptive non-uniform metal foam arrangement (case B and C), representing the inhomogeneity of the melting rate throughout the melting process in the inner, middle and outer regions. It was well-known that a smaller melting evenness
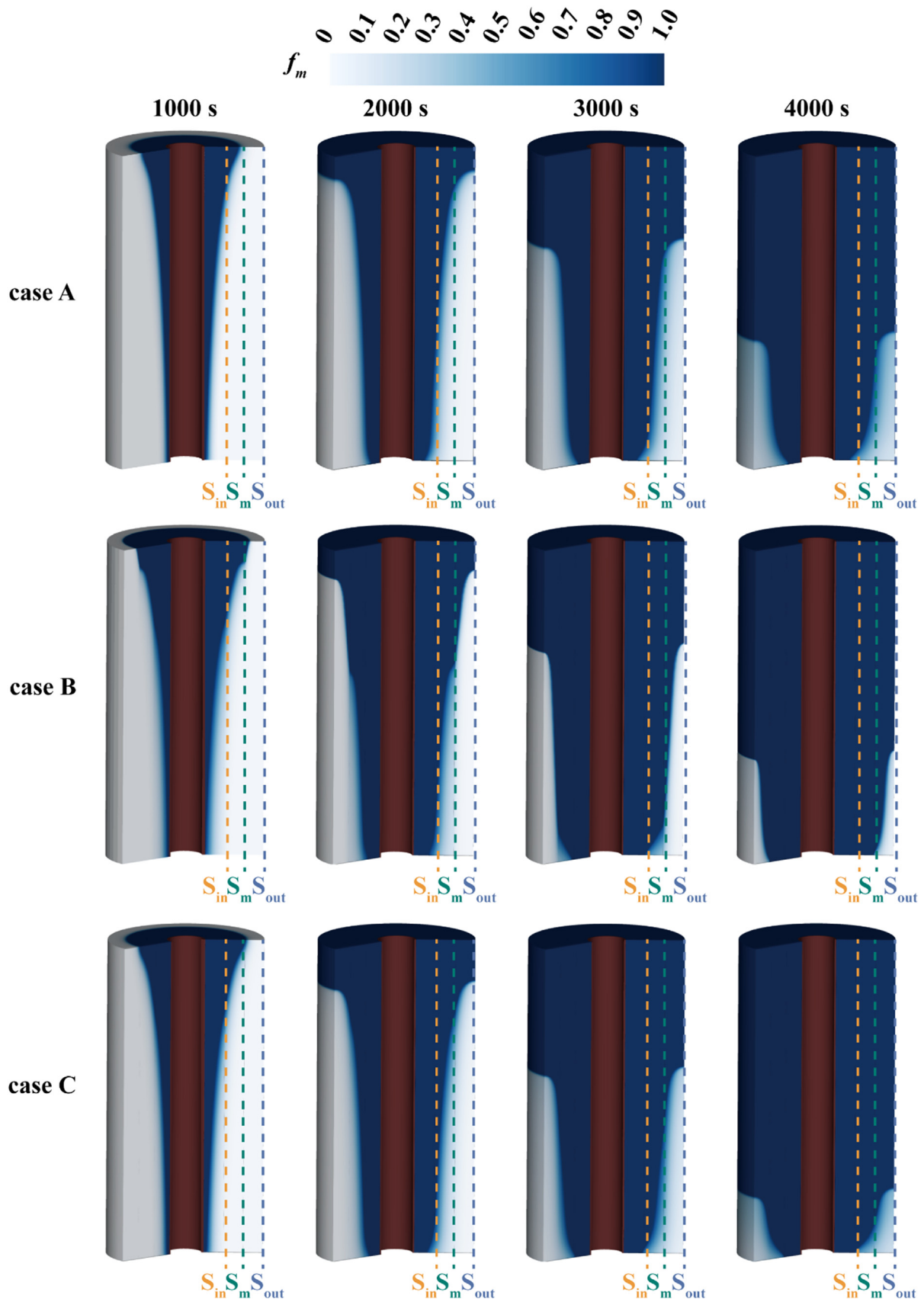
Fig. 8. Phase change behavior of vertical TES tube with uniform (case A) and adaptive non-uniform metal foam arrangement (case B and C) at t = 1000 s, 2000 s, 3000 s and 4000 s
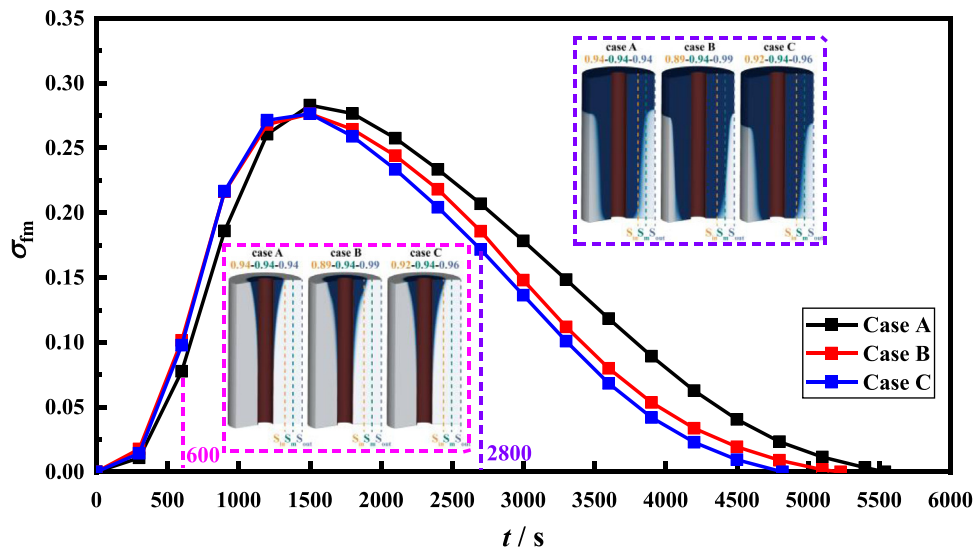
Fig. 9. Melting evenness index σ_{f_m} of vertical TES tube with uniform (case A) and adaptive non-uniform metal foam arrangement (case B and C)

index meant better melting performance with the more synchronized melting behavior. As Fig. 6 shown, more solid paraffin was present in case A at the initial stage of the charging ($t = 600$ s as an example), that was, the melting development was slow in all regions. Therefore, the smaller melting uniformity index in the early stage could not really confirm that case A was better than the other cases, but just showed that the overall melting development of case A was bad, based on the comprehensive analysis of Figs. 6 and 7. For subsequent development stages of the melting process ($t = 2800$s as an example), case C showed the most prominent consistency of melting behavior. It was reflected that adaptive metal foam arrangement in case C could better match the phase change heat transfer features of different regions based on the comprehensive strengthened effect of heat conduction and natural convection to the maximization.

4.2. Temperature distribution

To better illustrate the enhancement of adaptive non-uniform metal foam arrangement on phase change heat transfer, the temperature distribution of PCM regions is shown in Fig. 10. At $t = 1000$s, the temperature of the PCM only rose to the melting point in the region close to HTT. As the melting ($t = 2000$ s), thermal stratification appeared in case B and case C due to the appearance of a large amount of liquid PCM, while the overall temperature of the PCM region in case A was still at a low level. For $t = 3000$ s and 4000 s, the liquid phase PCM performed sensible heat storage, while the solid phase PCM performed latent heat storage, which resulted in thermal stratification manifested as higher in the top region than in the bottom region in all TES tubes. The thermal stratification in PCM followed the convection direction and was generated due to strong natural convection. The flow of high temperature liquid PCM under natural convection contributed to the thermal transport during the phase change throughout the TES tube. It was worth noting that only in case A, the thermal delamination was also reflected in the radial direction, which illustrated the poor performance of uniform metal foam in overcoming radial thermal resistance. Thermal delamination in the radial direction was an important problem that hindered the thermal transport of the overall TES, notably the melting of the outer region, so the adaptive non-uniform metal foam arrangement (case B and C) was proposed. It could be seen more clearly that case B and case C had nearly parallel isotherms, while case A had inclined isotherms.

It could be also found that at the same time, the vertical TES tube with adaptive non-uniform metal foam arrangement (case B and C) could achieve more thermal energy storage than that of case A, which was the most important factors for designing a more effective TES system, favoring the potential for further advances in TES applications.

To quantitatively demonstrate the effect of the metal foam morphology on local thermal transport, the transient average temperature and integral average temperature response rate of total PCM region and three subregions were depicted in Fig. 9. The transient average temperature was calculated by an area-average temperature of CFPCM domain. The integral average temperature response rate $\overline{RR}$ was adopted for characterizing average rate of temperature change over the entire melting process, which was expressed by:

$$\overline{RR} = \int_0^{t_{full}} \frac{1}{t_{full}} \frac{T(t_i) - T(t_{i-1})}{(t_i - t_{i-1})} dt \tag{17}$$

where $T(t_i)$ and $T(t_{i-1})$ were the temperatures at t_i and t_{i-1}.

It could be indicated in Fig. 11(a) – (d) that both case B and case C had higher temperature and thermal response than that of case A at every time, both for the whole region and for any subregion. As mentioned in Fig. 10 and Fig. 11, it was also observed by the higher temperature at the final moment that adaptive non-uniform metal foam arrangement could led to higher temperature, that was greater thermal volume, with the more sensible thermal energy with same latent thermal energy. Compared with the traditional uniform structure [46], the improvement of integral average temperature response rate as maximally much as 16.26 % was achieved by the metal structure of 0.92–0.94–0.96. It was verified that compared the case A [46], melting properties of inside, intermediate and outside subregions in case C could result in the heat transfer acceleration of 16.02 %, 16.38 % and 16.39 %, respectively.

4.3. Flow characteristic

Fig. 12 showed velocity field of vertical TES tube with uniform (case A) and adaptive non-uniform metal foam arrangement (case B and C) at $t = 1000$ s, 2000 s, 3000 s and 4000 s. With the appearance of melted paraffin, affected by the uneven temperature distribution, the liquid paraffin produced a flow under the action of the gravitational field, resulting in natural convection. Natural convection played a key role in phase change heat transfer, especially in PCM regions far from heat source (HTT). When $t = 1000$s, melt-
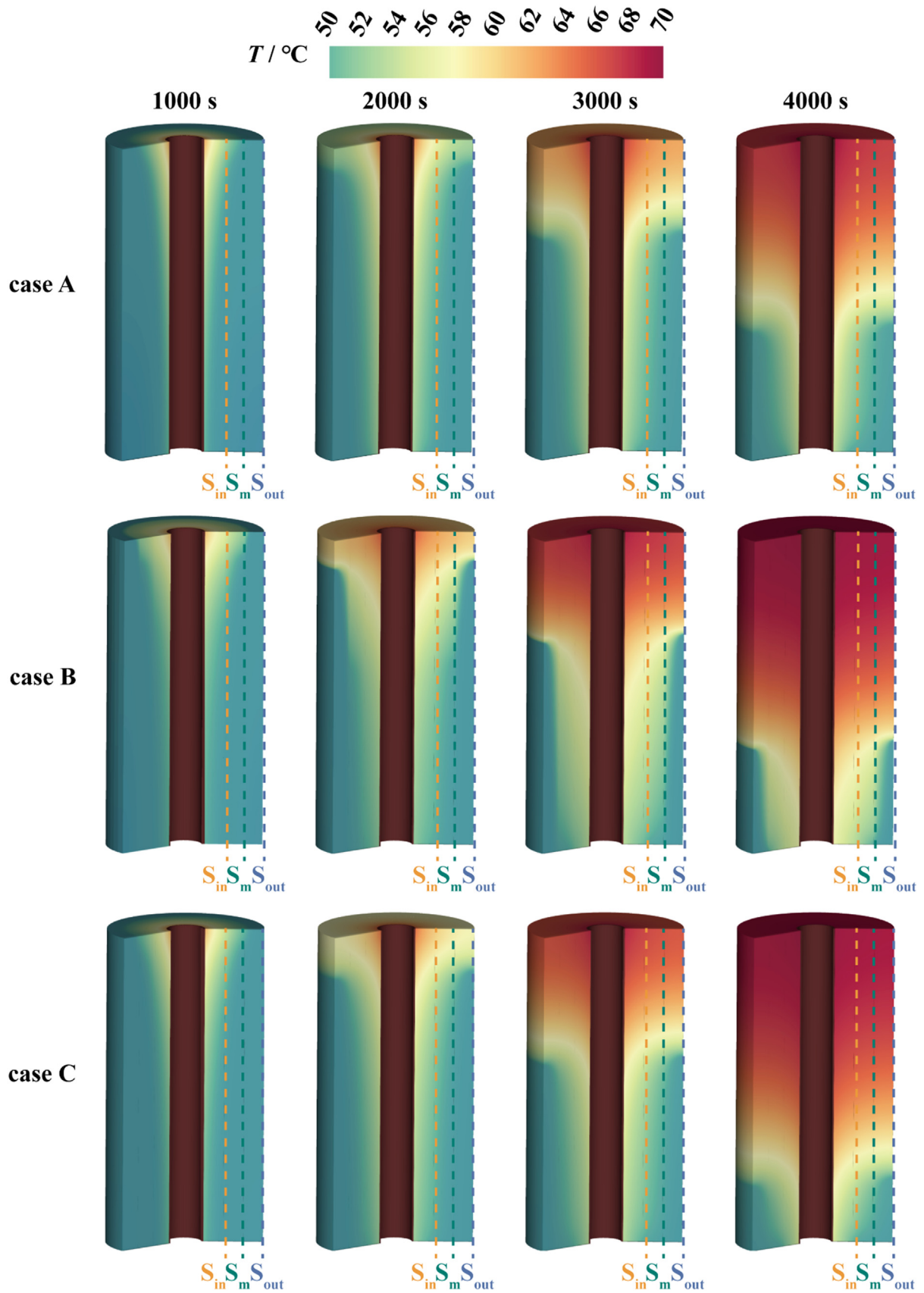
Fig. 10. Temperature evolution of vertical TES tube with uniform (case A) and adaptive non-uniform metal foam arrangement (case B and C) at t = 1000 s, 2000 s, 3000 s and 4000 s

ing had occurred in the area immediately adjacent to the HTT, and there was stronger natural convection along the wall of the HTT than at a distance. Case B and case C had wider and longer flow regions than case A. At the same time, it was observed that high velocity regions at the solid-liquid interface, which were generated by liquid paraffin flow scouring. With the appearance of more and more liquid paraffin, the flow range of liquid paraffin became larger and larger, gradually extending axial downward and radial outward, as shown in $t = 2000$ s, 3000 s. Liquid paraffin flowing in case B and case C can flow more quickly to the bottom and outer regions of the vertical TES tube. The rapid development of natural convection will be beneficial to the whole melting process. At $t = 4000$ s, the velocity of liquid paraffin at the phase interface in case A was significantly lower than that in case B and case C, where weak natural convection led to poor heat transfer performance, which was not conducive to the melting of solid paraffin in the outer bottom.

Velocity vector and vorticity contour of vertical TES tube with uniform (case A) and adaptive non-uniform metal foam arrangement (case B and C) at $t = 1000$ s, 2000 s, 3000 s and 4000 s were shown in Fig. 13. Vorticity was adopted for describing vortex motion and was defined as the curl of the fluid velocity vec-

tor. There were many vortices of different sizes in liquid paraffin. Vortices brought about more intense thermal disturbances, resulting in the more forceful natural convection, which could stimulate melting development. As melting developed, liquid paraffin particles flowed, rotated, and moved, visually demonstrating the development of natural convection. Meanwhile, it was observed that the front interface of the vorticity cloud image and the phase interface morphology extended in the axial and radial directions were consistent, which shows that natural convection played an important role in the development of the phase transition process. The vorticity distribution in the liquid region characterizes the flow strength of the liquid paraffin particles, and the vorticity at the solid-liquid interface could reflect the velocity gradient. At $t = 1000$s, the area where natural convection occurred in case A was smaller than that in case B and case C, and the growth and development of vortices was weak and slow. When $t = 2000$s and 3000 s, compared with case A, the vorticity in case C became stronger and stronger due to more liquid paraffin and proper porosity, resulting in the higher vorticity. Because natural convection was affected by the flow resistance generated by the metal foam skeleton, vortex development in the inside subregion of case B was limited, as shown in vorticity contour. At $t = 4000$ s, case B benefited from the minimum flow
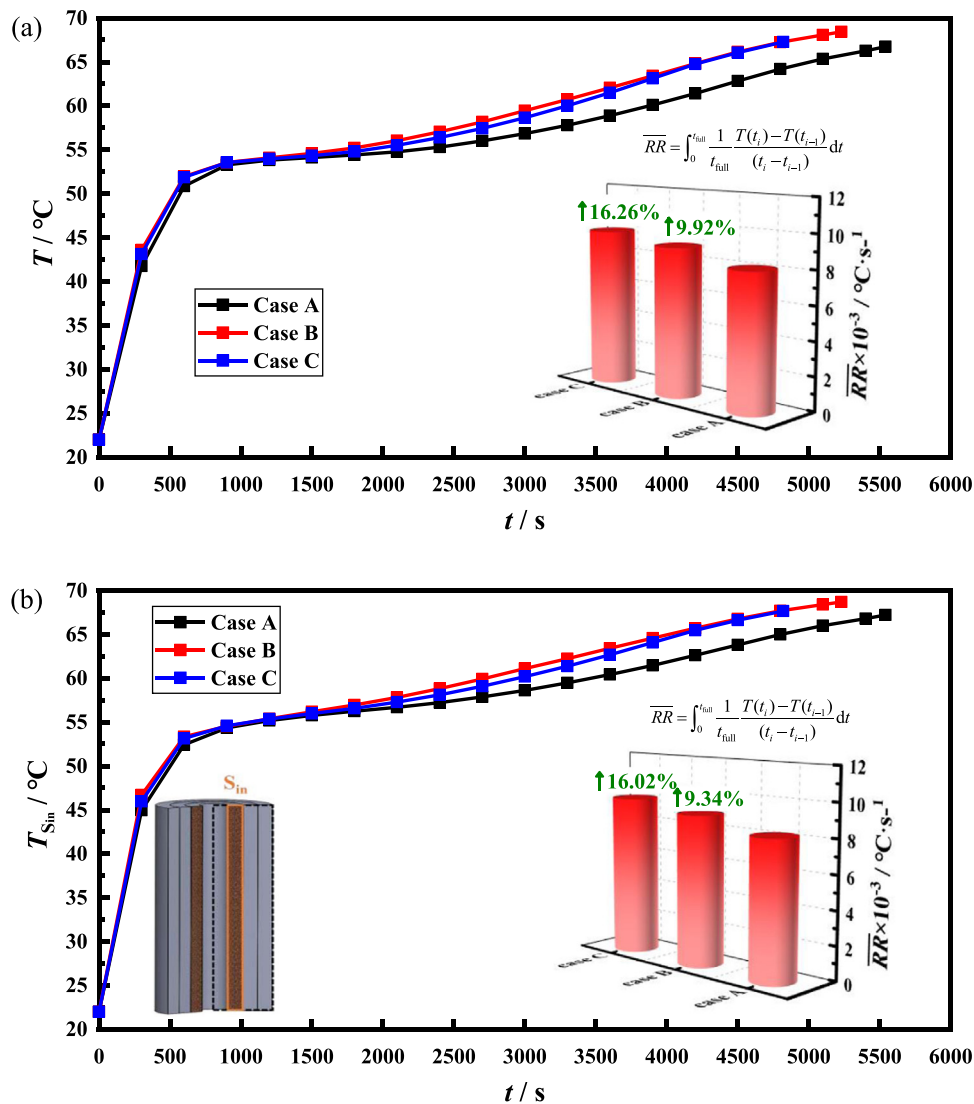

Fig. 11. Transient average temperature (T / °C) and integral average temperature response rate ($\overline{RR}$ / °C·s^{-1}) of (a) total PCM region, (b) S_{in}, (c) S_m and (d) S_{out} in vertical TES tube with uniform (case A) and adaptive non-uniform metal foam arrangement (case B and C)

(c)

$$\overline{RR} = \int_0^{t_{full}} \frac{1}{t_{full}} \frac{T(t_i) - T(t_{i-1})}{(t_i - t_{i-1})} dt$$

(d)

$$\overline{RR} = \int_0^{t_{full}} \frac{1}{t_{full}} \frac{T(t_i) - T(t_{i-1})}{(t_i - t_{i-1})} dt$$
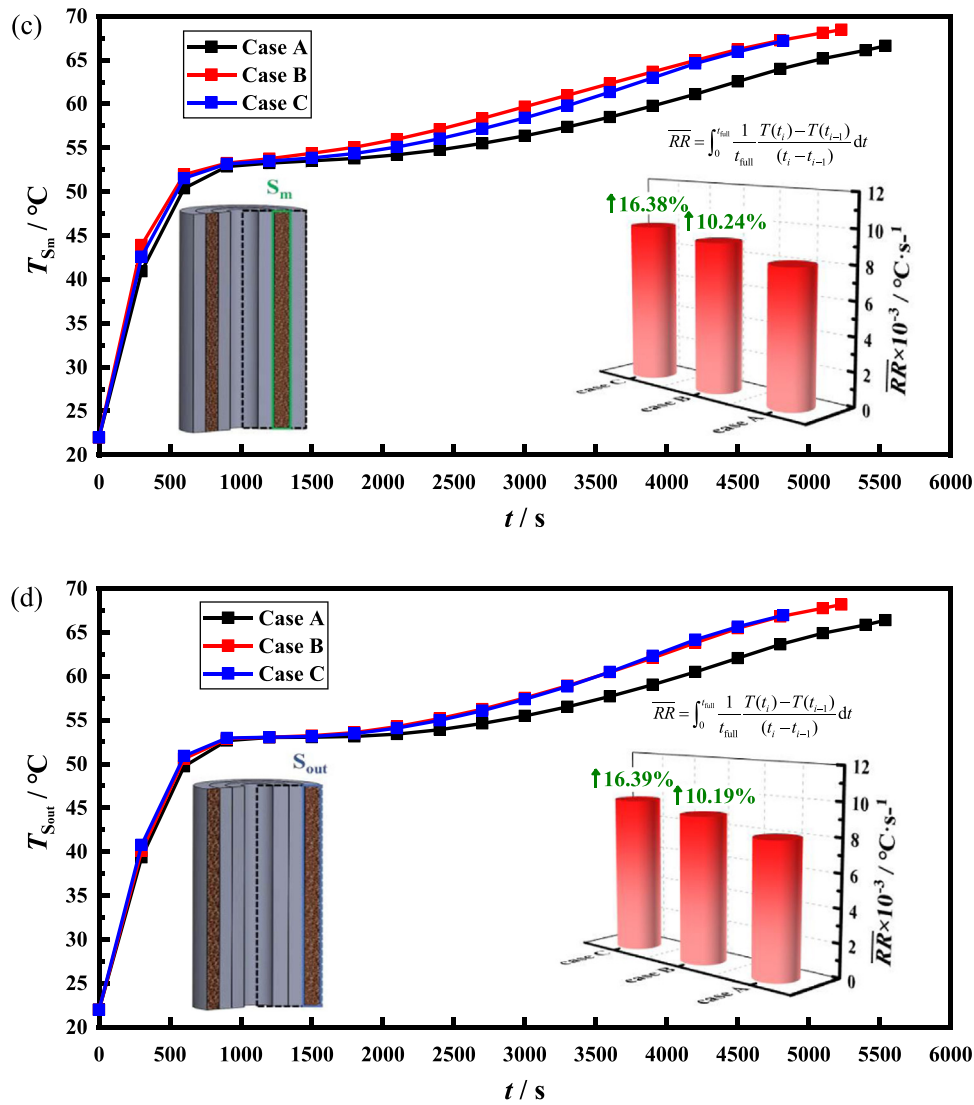
Fig. 11. Continued

resistance due to a greater porosity of 0.99 than others, achieved the stronger vorticity in the solid liquid phase interface of outside subregion, which indicated the greater velocity gradient causing the greater erosion of solid-liquid front. While the flow in the inside and intermediate subregions was weak with smaller vorticity, which was limited by low porosity. So, the development of natural convection in the whole PCM region cannot be strengthened to the maximum extent in case B. But for case C, due to optimal non-uniform metal foam arrangement, the development and movement of vortices in the whole PCM region in both axial and radial directions showed significant advantages compared with case A and case B.

4.4. Heat flux

Heat flux is one of the most important melting characteristics for thermal energy storage tank, which could describe the transient heat transfer transient in PCM region. $\overline{q}$ is defined as follows:

$$\overline{q} = \frac{\int_0^{t_{full}} q dt}{t_{full}} \tag{18}$$

where t_{full} is total melting time. Fig. 14 depicts the transient heat flux q and average heat flux $\overline{q}$ of vertical TES tube with uniform

(case A) and adaptive non-uniform metal foam arrangement (case B and C). During the melting process, the uniform metal foam arrangement could lead to slower heat transfer compared with adaptive non-uniform metal foam arrangement before 2500 s. The case C as the optimized adaptive non-uniform metal foam arrangement could achieve 5.64% improvement of heat flux for the whole melting process.

The improvement of thermal performance in vertical TES tube including melting process and phase change heat transfer was demonstrated in comparison of case A, case B and case C, as shown in Figs. 5–14. It also mentioned the combined enhancement was caused through natural convection and heat conduction. To further discussion the reasons for the reinforcement, Fig. 15 showed the difference between the porosity of outside subregion and inside subregion, the average porosity, and the enhancement ratio ER of vertical TES tubes with adaptive non-uniform metal foam arrangement (case 2- case 18). The enhancement ratio associated with complete melting time was the ratio of the difference between gradient and uniform metal foam tube to original uniform metal foam tube, which was expressed as:

$$ER = \frac{t_{full-casei} - t_{full-case1}}{t_{full-case1}} \tag{19}$$

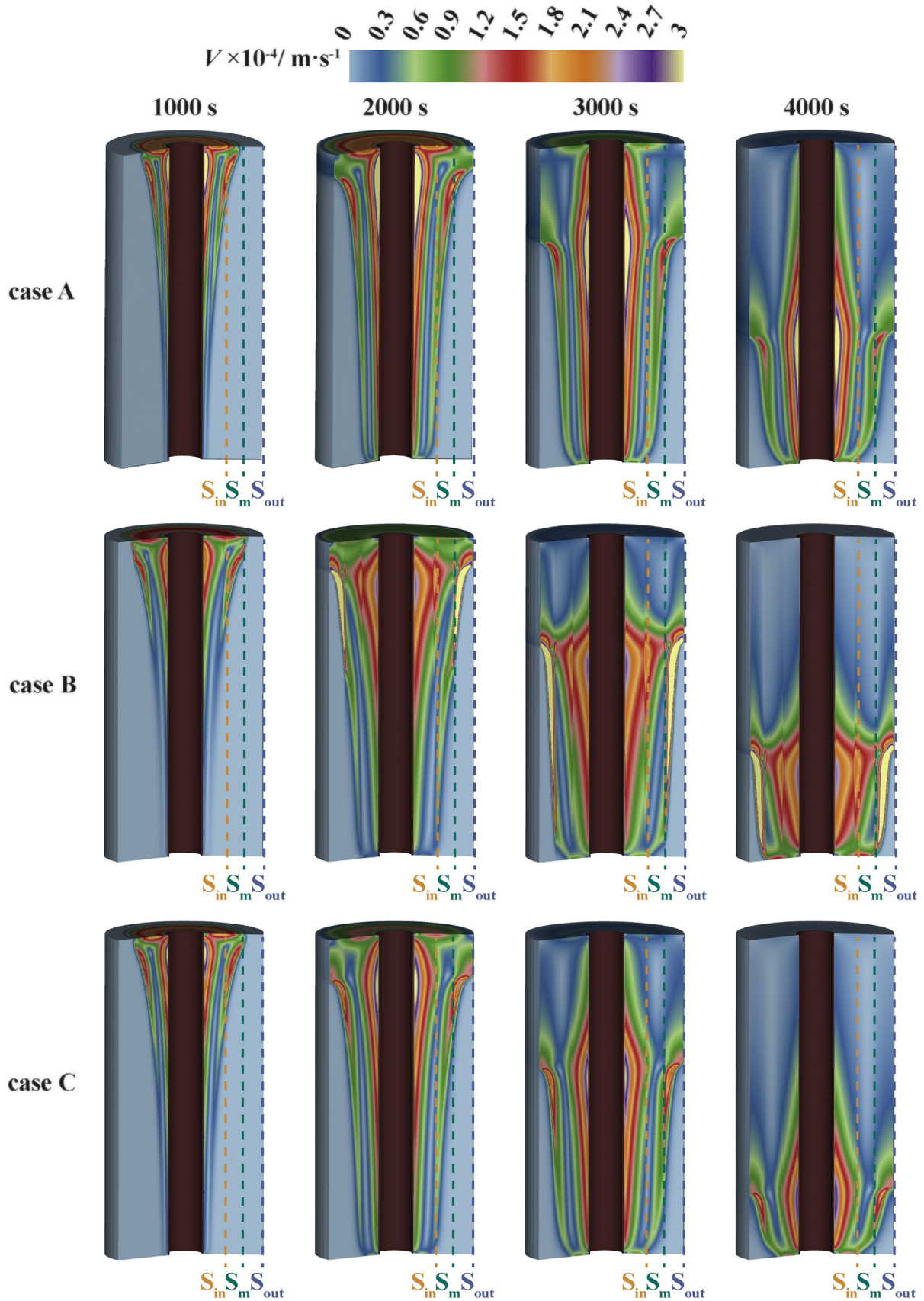**Fig. 12.** Velocity field of vertical TES tube with uniform (case A) and adaptive non-uniform metal foam arrangement (case B and C) at t = 1000 s, 2000 s, 3000 s and 4000 s

As shown in Fig. 15, the solid squares in yellow, pink, light green, blue, brown and gray represented the porosity gradients of non-uniform metal foam TES tubes of different groups, respectively. The red triangles represented the average porosity values of the entire PCM region for corresponding metal foam structures, while the green curve represented the melting rate enhancement rate. It was reported form the Fig. 15 that with the same porosity of intermediate subregion, the reduction of the difference of ε_{out} and ε_{in} led to the more significant enhance-

ment, which was resulted from the combination of heat conduction and natural convection of phase change thermal transport being strengthened. It was found that for the same porosity of inside subregion, the smaller difference between other subregions corresponded to the smaller average porosity was, the better the heat transfer performance was resulted in. But it was inevitable that the smaller porosity could occupy more space causing a reduction in latent thermal volume and make TES tube heavier and more expensive.
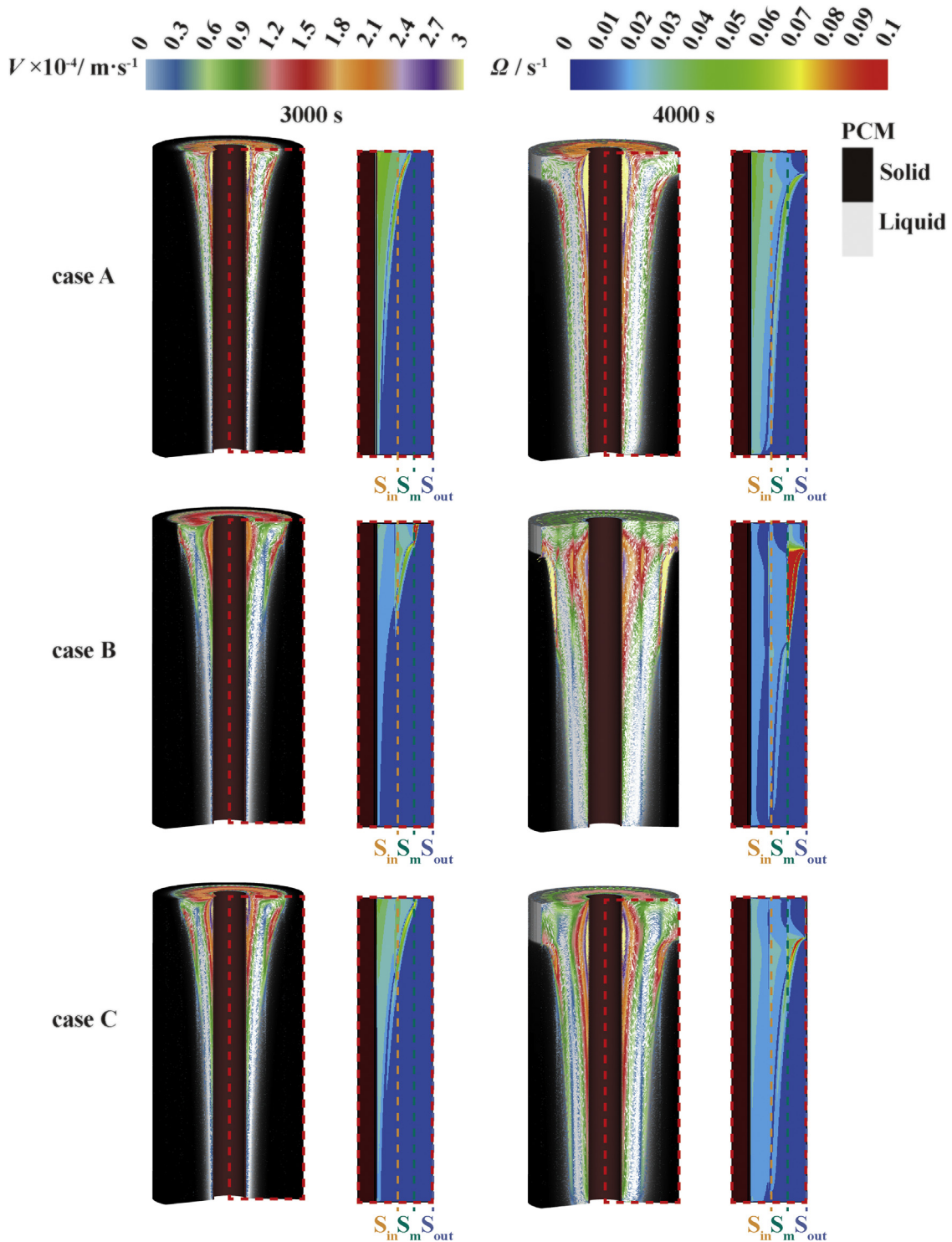

Fig. 13. Velocity vector and vorticity contour of vertical TES tube with uniform (case A) and adaptive non-uniform metal foam arrangement (case B and C) at $t = 1000$ s, 2000 s, 3000 s and 4000 s
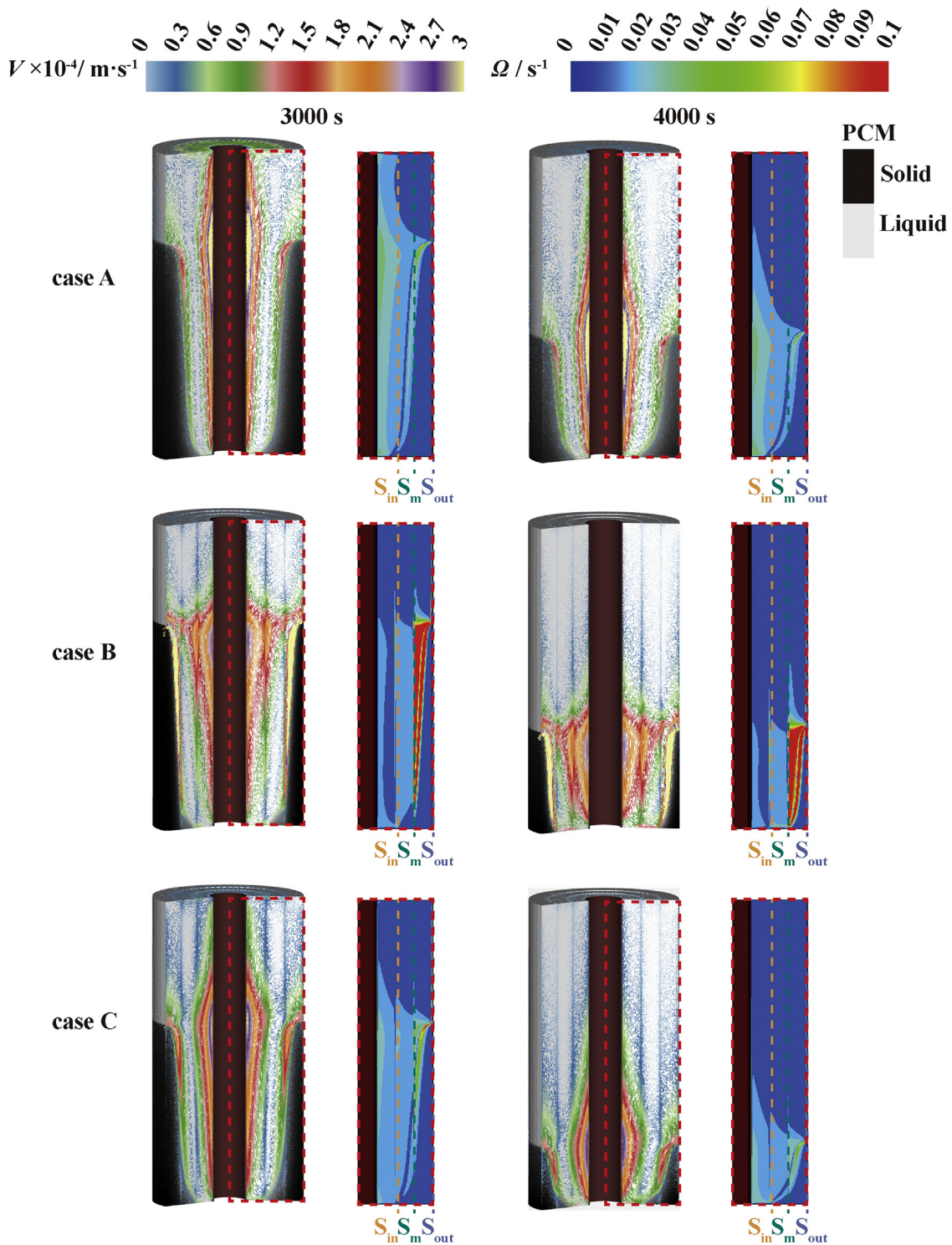
Fig. 13. Continued

Therefore, considering thermal capacity, weight and cost of TES tubes, 10 TES tubes filled with adaptive metal foam with average porosity of 0.94 (case 19-Case 28) were proposed to explore the adaptive arrangement strategy that can achieve the maximum strengthening of natural convection under the same heat conduction enhancement. These cases were divided into 5 groups according to the porosity of inside subregion, and metal foam structures were listed in Table 3.

Fig. 16 depicted melting time represented by bars and the porosity difference represented by solid square of vertical TES tube with the same average porosity of 0.94. It was demonstrated that the adaptive non-uniform metal foam arrangement with structure of 0.87–0.94–0.97 (case 19) was the most optimal design. Case 19 with the porosity difference of 0.1 reached the minimum melting time of 4590 s, which achieved the maximization of natural convection under the average porosity of 0.94, resulting a reduction
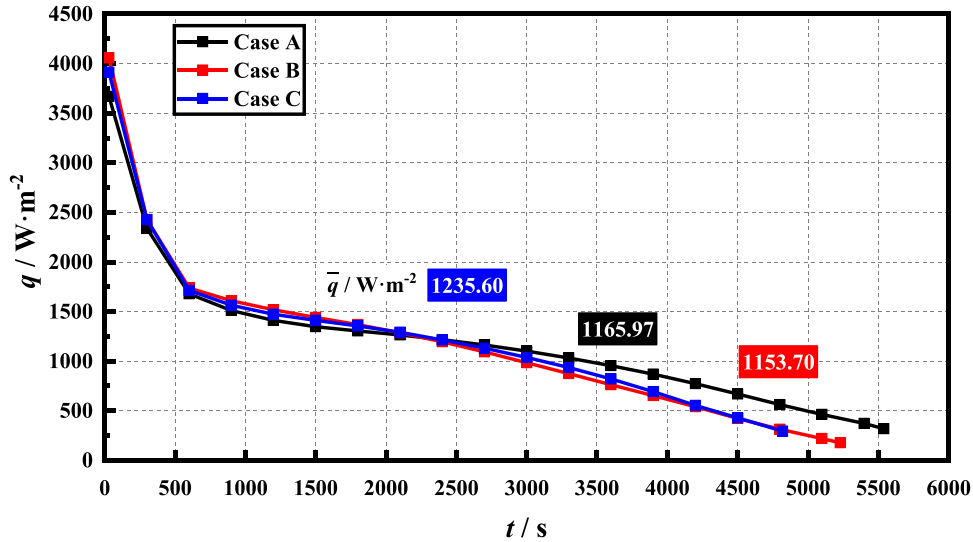
Fig. 14. Heat flux (q / W·m^{-2}) and average heat flux ($\bar{q}$ / W·m^{-2}) of vertical TES tube with uniform (case A) and adaptive non-uniform metal foam arrangement (case B and C)
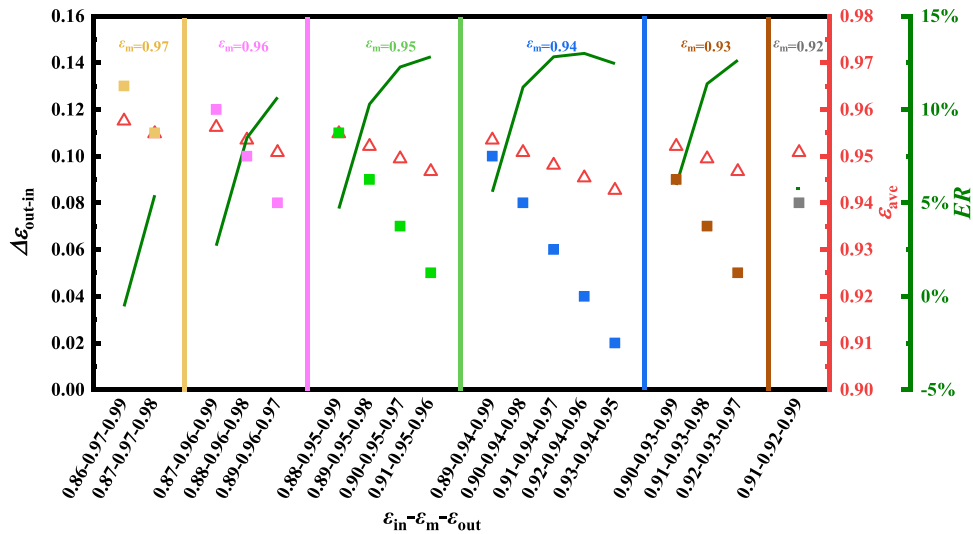

Fig. 15. The difference porosity between inside and outside region $\Delta\varepsilon_{out-in}$, the average porosity ε_{ave}, and the enhancement ratio (ER / %) of vertical TES tubes with adaptive non-uniform metal foam arrangement (case 2- case 18)

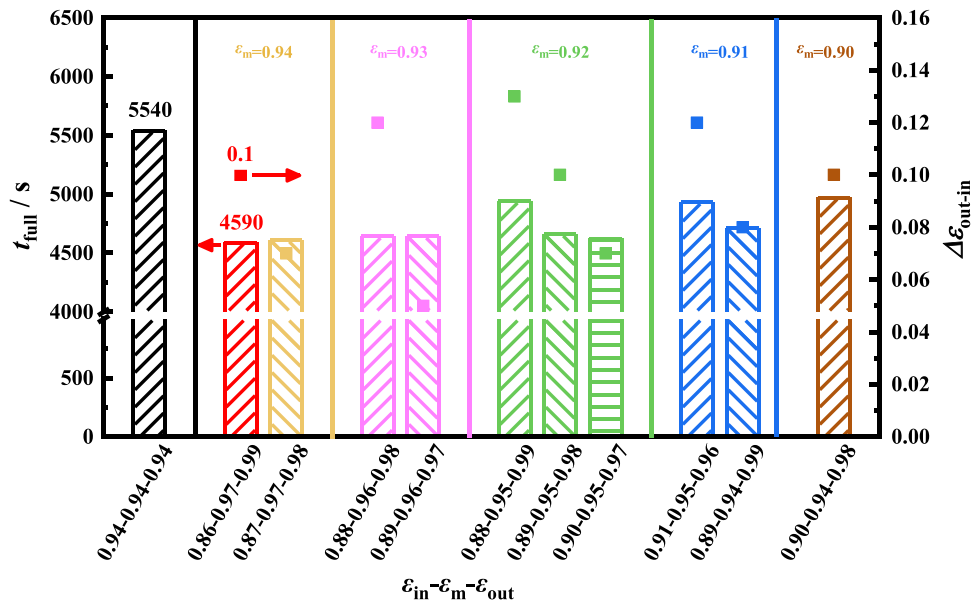**Fig. 16.** Melting time (t_{full} / s) and the difference porosity between inside and outside region $\Delta\varepsilon_{out-in}$ of vertical TES tube with the same average porosity ε_{ave}

Table 3
The metal foam porosity morphologies of adaptive metal foam arrangement with average porosity of 0.94.

	ε_{in}	ε_{m}	ε_{out}
case19	0.87	0.94	0.97
case20	0.89	0.94	0.96
case21	0.86	0.93	0.98
case22	0.91	0.93	0.96
case23	0.86	0.92	0.99
case24	0.88	0.92	0.98
case25	0.90	0.92	0.97
case26	0.87	0.91	0.99
case27	0.90	0.91	0.98
case28	0.89	0.90	0.99

as much as 17.15 % of complete melting time, compared with the traditional uniform structure [46]. It was revealed that the greater heat transfer enhancement t was achieved by the adaptive metal foam arrangement with the larger intermediate porosity and the larger porosity difference of inside and outside porosity, which has shown great potentiality for the efficient vertical metal foam TES system as light and as economical as possible, also avoiding at the expense of thermal energy capacity.

5. Conclusion

A series of numerical outcomes were carried out to investigate optimization of adaptive metal foam arrangement for vertical TES tube. Firstly, a two-dimensional symmetric simulation model, validated by the experimental results, of vertical TES tube impregnated with paraffin and metallic foam with varied porosity (case 2-case 18) was conducted to compared to uniform structure (case 1). Then, the homogeneity of melting fraction and temperature, progression of the melt front, temperature distribution were provided for analysis the synthetic optimization of natural convection and heat conduction. In addition, graded metal foam structures (case 19- case 28) with the same average porosity were proposed and discussed for exploring the maximum enhancement of natural convection under the same heat conduction enhancement. Conclusions were drawn as follows:

(1) In the adaptive metallic foam arrangement with increasing porosity gradient from inside to outside, for the same porosity of intermediate subregion, the properly smaller difference between inside and outside subregions corresponded to the smaller average porosity was, the better the heat transfer performance was resulted in, which caused from the combination of heat conduction and natural convection of phase change heat transfer being strengthened. Compared with the uniform design, the metal foam structure (0.92–0.94–0.96) could achieve the reduction of the charging time by 13.00 % and the improvement of integral average temperature response rate as much as 16.26 %. More intense natural convection with stronger liquid paraffin vortex could be obtained by adaptive metallic foam arrangement.

(2) Considering that the smaller average porosity of the whole TES tube could occupy more space causing a reduction in latent thermal volume and make TES tube heavier and more expensive, the numerical results about adaptive metal foam with the same average porosity indicated the greater heat transfer enhancement was achieved by the larger intermediate porosity and the larger porosity difference of inside and outside porosity.

(3) Directed by the optimized adaptive metal foam arrangement strategy, the optimization of vertical thermal energy storage tube could significantly shorten the melting duration as maximal as 17.15% in comparison to the original uniform design,

which contributed to the design of the efficient vertical metal foam TES system as light and as economically efficient as possible, without sacrificing the expense of thermal energy capacity.

Declaration of Competing Interest

The authors declare that they have no known competing financial interests or personal relationships that could have appeared to influence the work reported in this paper.

CRediT authorship contribution statement

Junfei Guo: Software, Data curation, Validation, Formal analysis, Visualization, Methodology, Writing – original draft, Writing – review & editing. **Ze Li:** Investigation, Methodology, Data curation, Visualization. **Pan Wei:** Methodology, Validation, Data curation. **Ling Li:** Validation, Writing – review & editing. **Xiaohu Yang:** Conceptualization, Resources, Methodology, Supervision, Writing – original draft, Writing – review & editing. **Ya-Ling He:** Resources, Methodology, Supervision, Writing – original draft, Writing – review & editing. **Kamel Hooman:** Conceptualization, Supervision, Writing – original draft, Writing – review & editing.

Data availability

Data will be made available on request.

References

[1] Y. Xiang, Z. Xie, S. Furbo, D. Wang, M. Gao, J. Fan, A comprehensive review on pit thermal energy storage: technical elements, numerical approaches and recent applications, J. Energy Storage 55 (2022) 105716.

[2] A. Lyden, C.S. Brown, I. Kolo, G. Falcone, D. Friedrich, Seasonal thermal energy storage in smart energy systems: district-level applications and modelling approaches, Renew. Sustain. Energy Rev. 167 (2022) 112760.

[3] L. Cirocco, P. Pudney, S. Riahi, R. Liddle, H. Semsarilar, J. Hudson, et al., Thermal energy storage for industrial thermal loads and electricity demand side management, Energy Convers. Manage. 270 (2022) 116190.

[4] H.S. Yu, H. Helland, X.J. Yu, T. Gundersen, G. Sin, Optimal design and operation of an Organic Rankine Cycle (ORC) system driven by solar energy with sensible thermal energy storage, Energy Convers. Manage. 244 (2021) 114494.

[5] S. Riahi, M. Liu, R. Jacob, M. Belusko, F. Bruno, Assessment of exergy delivery of thermal energy storage systems for CSP plants: cascade PCMs, graphite-PCMs and two-tank sensible heat storage systems, Sustain. Energy Techn. 42 (2020) 100823.

[6] X.Z. Zhang, Y.T. Ren, Y. Ren, Y.Y. Yan, A novel bionic packed bed latent heat storage system filled with encapsulated PCM for thermal energy collection, Therm. Sci. Eng. Prog. 35 (2022) 101449.

[7] D.W. Zhang, C.L. Fang, X. Qin, H. Li, H. Liu, X.H. Wu, Performance study of transcritical CO2 heat pump integrated with ejector and latent thermal energy storage for space heating, Energy Convers. Manage. 268 (2022) 115979.

[8] C. Susantez, Numerical investigation of latent heat thermal energy storage unit with different configurations and phase change materials, J. Energy Storage 54 (2022) 105279.

[9] K. Walayat, J. Duesmann, T. Derks, A. houshang Mahmoudi, R. Cuypers, M. Shahi, Experimental and numerical investigations for effective thermal conductivity in packed beds of thermochemical energy storage materials, Appl. Therm. Eng. 193 (2021) 117006.

[10] C. Wang, H. Yang, B. Nie, B. Zou, Z. Li, J. Han, et al., Discharging behavior of a shell-and-tube based thermochemical reactor for thermal energy storage: modeling and experimental validation, Int. J. Heat Mass Transf. 183 (2022) 122160.

[11] Q.Q. Xin, J.S. Xiao, T.Q. Yang, H.Y. Zhang, X. Long, Thermal management of lithium-ion batteries under high ambient temperature and rapid discharging using composite PCM and liquid cooling, Appl. Therm. Eng. 210 (2022) 118230.

[12] H.M.T. Al-Najjar, J.M. Mahdi, D.O. Bokov, N.B. Khedher, N.K. Alshammari, M.J.C. Opulencia, et al., Improving the melting duration of a PV/PCM system integrated with different metal foam configurations for thermal energy management, Nanomater.-Basel 12 (2022) 423.

[13] C. Yu, J. Park, J.R. Youn, Y.S. Song, Sustainable solar energy harvesting using phase change material (PCM) embedded pyroelectric system, Energy Convers. Manage. 253 (2022) 115145.

[14] Z.A. Nawsud, A. Altouni, H.S. Akhijahani, H. Kargarsharifabad, A comprehensive review on the use of nano-fluids and nano-PCM in parabolic trough solar collectors (PTC), Sustain. Energy Techn. 51 (2022) 101889.

[15] A.A. Ghoneim, Comparison of theoretical models of phase-change and sensible heat storage for air and water-based solar heating systems, Sol. Energy 49 (1989) 209–220.

[16] X. Huang, F. Li, T. Xiao, J. Guo, F. Wang, X. Gao, X. Yang, He Y-L. Investigation and optimization of solidification performance of a triplex-tube latent heat thermal energy storage system by rotational mechanism, Appl. Energy 331 (2022) 120435.

[17] F. Li, X. Huang, Y. Li, L. Lu, X. Meng, X. Yang, B Sundén, Application and analysis of flip mechanism in the melting process of a triplex-tube latent heat energy storage unit, Energy Report. 9 (2023) 3989–4004.

[18] M.A. Dekhil, J.V. Simo Tala, O. Bulliard-Sauret, D Bougeard, Numerical analysis of the effect of the iso-surface fin redistribution on the performance enhancement of a shell-and-tube latent heat thermal energy storage unit for low-temperature applications, J. Energy Storage 56 (2022) 105892.

[19] L. Liu, Q. Zhang, Z. Zhai, X. Zhao, A simplified method to simulate tube-in–tank latent thermal energy storage with fin-enhanced phase change material in data center, J. Energy Storage 55 (2022) 105757.

[20] H. Zhang, X. Li, L. Liu, T. Ma, Q. Wang, J Liu, Experimental investigation on paraffin melting in high porosity copper foam under centrifugal accelerations, Appl. Therm. Eng. 178 (2020) 115504.

[21] M. Hassani Soukht Abandani, D. Domiri Ganji, Melting effect in triplex-tube thermal energy storage system using multiple PCMs-porous metal foam combination, J. Energy Storage 43 (2021) 103154.

[22] M.M. Heyhat, S. Mousavi, M. Siavashi, Battery thermal management with thermal energy storage composites of PCM, metal foam, fin and nanoparticle, J. Energy Storage 28 (2020) 101235.

[23] M. Aramesh, B. Shabani, Metal foams application to enhance the thermal performance of phase change materials: a review of experimental studies to understand the mechanisms, J. Energy Storage 50 (2022) 104650.

[24] M. Aramesh, B. Shabani, Metal foam-phase change material composites for thermal energy storage: a review of performance parameters, Renew. Sustain. Energy Rev. 155 (2022) 111919.

[25] S. Rahmanian, M. Moein-Jahromi, H. Rahmanian-Koushkaki, K. Sopian, Performance investigation of inclined CPV system with composites of PCM, metal foam and nanoparticles, Sol. Energy 230 (2021) 883–901.

[26] P.T. Sardari, R. Babaei-Mahani, D. Giddings, S. Yasseri, M.A. Moghimi, H. Bahai, Energy recovery from domestic radiators using a compact composite metal Foam/PCM latent heat storage, J. Clean. Prod. 257 (2020) 120504.

[27] A. Wazeer, A. Das, C. Abeykoon, A. Sinha, A. Karmakar, Phase change materials for battery thermal management of electric and hybrid vehicles: a review, Energy Nexus 7 (2022) 100131.

[28] W.Q. Li, Z.G. Qu, Y.-.L. He, Y.B. Tao, Experimental study of a passive thermal management system for high-powered lithium ion batteries using porous metal foam saturated with phase change materials, J. Power Source. 255 (2014) 9–15.

[29] Z. Wang, J. Wu, D. Lei, H. Liu, J. Li, Z Wu, Experimental study on latent thermal energy storage system with gradient porosity copper foam for mid-temperature solar energy application, Appl. Energy 261 (2020) 114472.

[30] N. Prasanth, M. Sharma, R.N. Yadav, P. Jain, Designing of latent heat thermal energy storage systems using metal porous structures for storing solar energy, J. Energy Storage 32 (2020) 101990.

[31] H.M. Ali, An experimental study for thermal management using hybrid heat sinks based on organic phase change material, copper foam and heat pipe, J. Energy Storage 53 (2022) 105185.

[32] A. Veismoradi, A. Modir, M. Ghalambaz, A. Chamkha, A phase change/metal foam heatsink for thermal management of battery packs, Int. J. Therm. Sci. 157 (2020) 106514.

[33] G. Liu, Z. Du, T. Xiao, J. Guo, L. Lu, X. Yang, K. Hooman, Design and assessments on a hybrid pin fin-metal foam structure towards enhancing melting heat transfer: an experimental study, Int. J. Therm. Sci. 182 (2022) 107809.

[34] A. Kumar, S.K. Saha, Latent heat thermal storage with variable porosity metal matrix: a numerical study, Renew. Energy 125 (2018) 962–973.

[35] G. Liu, T. Xiao, J. Guo, P. Wei, X. Yang, K. Hooman, Melting and solidification of phase change materials in metal foam filled thermal energy storage tank: evaluation on gradient in pore structure, Appl. Therm. Eng. 212 (2022) 118564.

[36] T. Xiao, G. Liu, J. Guo, G. Shu, L. Lu, X Yang, Effect of metal foam on improving solid–liquid phase change in a multi-channel thermal storage tank, Sustain. Energy Technol. Assessm. 53 (2022) 102533.

[37] J.M. Mahdi, E.C. Nsofor, Multiple-segment metal foam application in the shell-and-tube PCM thermal energy storage system, J. Energy Storage 20 (2018) 529–541.

[38] A. Ghahremannezhad, H. Xu, M.R. Salimpour, P. Wang, K. Vafai, Thermal performance analysis of phase change materials (PCMs) embedded in gradient porous metal foams, Appl. Therm. Eng. 179 (2020) 115731.

[39] G.K. Marri, C. Balaji, Experimental and numerical investigations on the effect of porosity and PPI gradients of metal foams on the thermal performance of a composite phase change material heat sink, Int. J. Heat Mass Transf. 164 (2021) 120454.

[40] Y. Zhuang, Z. Liu, W. Xu, Effects of gradient porous metal foam on the melting performance and energy storage of composite phase change materials subjected to an internal heater: a numerical study and PIV experimental validation, Int. J. Heat Mass Transf. 183 (2022) 122081.

[41] H. Ami Ahmadi, N. Variji, A. Kaabinejadian, M. Moghimi, M Siavashi, Optimal design and sensitivity analysis of energy storage for concentrated solar power plants using phase change material by gradient metal foams, J. Energy Storage 35 (2021) 102233.

[42] Z. Du, G. Liu, X. Huang, T. Xiao, X. Yang, Y.-.L He, Numerical studies on a fin–foam composite structure towards improving melting phase change, Int. J. Heat Mass Transf. 208 (2023) 124076.

[43] M. Fadl, P.C. Eames, Numerical investigation of the influence of mushy zone parameter Amush on heat transfer characteristics in vertically and horizontally oriented thermal energy storage systems, Appl. Therm. Eng. 151 (2019) 90–99.

[44] A. Žukauskas, Heat transfer from tubes in crossflow, Adv. Heat Transf. 8 (1972) 93–160.

[45] V. Calmidi, Transport Phenomena in High Porosity Fibrous Metal Foams, University of Colorado, Boulder, CO, 1998.

[46] J. Guo, P. Wei, X. Huang, X. Yang, Y.-.L. He, B. Sundén, Radially graded metal foams arrangement in heat storage device of photothermal utilization systems, Sol. Energy Mater. Sol. Cells 256 (2023) 112315.